Journal of
Materials Chemistry A

Materials for energy and sustainability

Accepted Manuscript

This article can be cited before page numbers have been issued, to do this please use: D. Wei, P. H. Ho, A. Noreen, O. Pajalic, L. Josefsson, L. Olsson and D. Creaser, *J. Mater. Chem. A*, 2026, DOI: 10.1039/D6TA00959J.

ROYAL SOCIETY OF CHEMISTRY

rsc.li/materials-a

View Article Online
DOI: 10.1039/D6TA00959J

ARTICLE

Investigation of the dynamic active center for CO_2 hydrogenation to light olefins over Na-modified iron catalysts

Received 00th January 2026,
Accepted 00th January 20xx

DOI: 10.1039/x0xx00000x

Wei Di [a], Phuoc Hoang Ho [a], Aqsa Noreen [a], Oleg Pajalic [b], Lars Josefsson [c], Louise Olsson [a,] * and Derek Creaser [a]

Alkali-modified iron catalysts often undergo phase transitions during CO_2 hydrogenation, leading to mixed products and lower reactivity. Further elucidating their active sites, concurrently suppressing by-products, and maintaining stability remain significant challenges. This work initially explores the reactivity of pure Fe_5C_2 and Fe_3O_4 nano-catalysts, followed by the regeneration of deactivated catalysts by syngas-induced carburization to evaluate the phase-dependent catalytic behavior. Subsequently, Na_2CO_3 dopant was added via solid-phase mixing or wet impregnation to modify the single-phase iron catalysts. The resulting active sites responsible for olefin formation were further investigated, and changes in CO selectivity were explored. The results confirm a particle size–dependent dynamic phase transition between the active Fe_5C_2 phase and the inactive Fe_3O_4 phase. This transition leads to an initial decline in catalytic activity, followed by stabilization toward a pseudo-steady state. The physical mixing of Fe_5C_2 and Na_2CO_3 significantly enhances selectivity for light olefins among hydrocarbons. However, the Na_2CO_3 additive also further promotes the oxidation of Fe_5C_2 to Fe_3O_4, enhancing water-gas shift activity. Additionally, Na_2CO_3 suppresses surface hydrogen dissociation, thereby preventing further CO conversion into olefins and long-chain products via the Fischer-Tropsch synthesis (FTS) reaction. Together, these effects result in higher CO selectivity during CO_2 hydrogenation over the Na_2CO_3-modified Fe_5C_2 catalyst. Operating at a low gas space velocity (GHSV) drastically reduces CO selectivity by promoting the CO-based FTS reactions; however, the associated high CO_2 conversion and elevated water partial pressure also promote and accelerate the oxidation of Fe_5C_2 to Fe_3O_4. These findings highlight that olefin formation originates at the iron carbide–alkali interface and that catalyst stability is governed by a complex interplay of phase transitions, alkali metal promoter effects, and reaction conditions. Moreover, the observed oxidation acceleration at low GHSV may aid in the rapid screening of stable iron-based catalysts in future studies.

1 Introduction

The use of captured CO_2 together with H_2 (obtained from sustainable electricity) to produce e-chemicals is a promising option for decarbonization of the chemical industry [1]. The production of light olefins (ethylene, propylene, and butene), which are important building blocks in the chemical and polymer industries, mostly relies on fossil resources in traditional processes such as naphtha steam cracking, alkane dehydrogenation, and fluid catalytic cracking (FCC) [2]. These traditional processes not only consume large amounts of fossil resources but also emit significant amounts of CO_2 [2,3]. If CO_2 can be used as a carbon source to produce olefins and then chemicals and plastics, both severe CO_2 emissions and fossil resource consumption can be avoided. Additionally, CO_2 can also be stored in many plastic commodities with long lifecycles [3]. However, due to the high thermodynamic stability of CO_2 and the significant external energy input required for its conversion, the value-added use of CO_2 has historically been limited to specialized industrial processes such as those in the fertilizer and food industries [4]. With the large-scale rise of renewable energy, especially the development of green hydrogen technologies that integrate solar and wind power with water electrolysis for green hydrogen production, the abundant supply of cheap hydrogen makes the valorization of CO_2 into value-added olefins via hydrogenation increasingly feasible [1-4].

Currently, there are two accessible pathways for the catalytic hydrogenation of CO_2 into olefins. One is the methanol-intermediated pathway, which employs a tandem catalyst system consisting of an oxide catalyst for converting CO_2 to methanol (CTM) and a zeolite component for the subsequent methanol-to-olefins (MTO) reaction [1, 4-8]. However, the efficiency of CO_2 conversion remains low, with a significant amount of CO as a by-product. This is primarily due to the mismatch between the optimal reaction conditions for the CTM and MTO reactions [8]. The iron-based Fischer-Tropsch synthesis (FTS) is another promising technology that can efficiently produce olefins from both CO_2 and CO. Over the iron catalyst containing various iron species (iron oxides/iron carbides), CO_2

[a] Chemical Engineering and Competence Centre for Catalysis, Chalmers University of Technology, Gothenburg 41296, Sweden.
[b] Perstorp Specialty Chemicals AB, Perstorp 28480, Sweden.
[c] Josefsson Sustainable Chemistry AB, Stenungsund 44448, Sweden.
* Corresponding author: louise.olsson@chalmers.se

View Article Online
DOI: 10.1039/D6TA00950J

hydrogenation is reported to proceed via two steps: the Reverse Water-Gas Shift (RWGS) reaction converting CO_2 to CO, followed by the FTS of CO to hydrocarbons [1, 4-7, 9-12]. Specifically, the iron magnetite (Fe_3O_4) component is generally regarded as the active site for CO formation in the RWGS reaction, while Hägg iron carbide (Fe_5C_2) serves as the primary phase catalyzing the FTS reactions [9-10]. Notably, iron phase transformations and surface reconstruction occur during CO_2 hydrogenation. In general, CO_2 and H_2O act as oxidizers that can oxidize iron carbide into iron oxides, while CO, H_2, and hydrocarbon products act as reducing and carburizing agents. As a result, variations in product composition and reactant atmosphere under different reaction conditions can easily induce complex phase changes between iron oxides and iron carbides within the catalyst [10-11].

Alkaline metal dopants (e.g., Na, K), acting as electronic and structural promoters, are commonly added to the iron catalyst to enhance higher olefin yields during the FTS process [9,12-19]. These additives are believed to increase the surface basicity of the catalyst [9,12-13], influence the formation of iron carbide [12-13], and decrease the H:C ratio on the iron carbide surface [14]. Consequently, they often modify the catalyst's activity, suppress CH_4 formation, and improve selectivity toward olefins. Numerous studies have investigated the effects of both single and mixed alkali metal promoters in iron catalysts for CO- or CO_2-based FTS reactions, with varying conclusions depending on the catalyst preparation method used [9,13,15-18]. For example, Na and K—introduced as cationic components of the precipitant (carbonate or hydroxide)—are typically incorporated into the precipitated iron catalyst during synthesis. Before CO_2 hydrogenation, the iron phase inside the catalyst was influenced by these alkaline elements during pre-carburizing by CO [17-18] or syngas [11,15], or reduction by H_2 treatment [9-10, 12-13,16]. It has been reported that these alkaline metal dopants enhance CO conversion and dissociation on the iron surface, while also increasing carbon deposition via the Boudouard reaction, resulting in higher amounts of iron carbide and coke in Na- or K-modified iron catalysts, which leads to increased CO_2 activation [9-10,13]. However, the inhibition of hydrogen dissociation by alkaline dopants can simultaneously reduce the overall CO_2 conversion rate [12, 14]. Additionally, some studies report that iron catalysts doped with alkaline metals enhance both the adsorption strength and adsorption capacity of CO_2 [13,19]. Nevertheless, since iron carbide and metallic iron catalysts are readily oxidized by CO_2 to iron oxide, increasing CO_2 adsorption may accelerate the phase transformation from iron carbide to iron oxides, thereby also weakening CO_2 conversion [10, 17].

So far, several fundamental questions regarding alkaline metal dopant-modified iron catalysts remain unresolved. In particular, there is a lack of detailed research on the active center responsible for CO_2 hydrogenation to light olefin while suppressing the formation of both CO and CH_4. A recent study reported that the active Fe_5C_2-K_2CO_3 interface, produced by the physical mixing of FeC_2O_4 and carbonaceous K with close proximity (mortar mixing with average particle size of 8 μm), can significantly enhance the olefins production during CO_2 hydrogenation, but other methods of integration resulted in either lower conversion of CO_2, or higher selectivity for CH_4 and CO, along with decreased selectivity for light olefins [9]. However, an in-depth study is still lacking on how the proximity between iron catalysts and alkaline metal dopants affects the catalyst's surface properties and active phase composition, thus ultimately leading to correlated changes in product distribution and catalytic activity.

In this work, pure nano-sized iron carbide (FeC_x) or iron magnetite (FeO_y) catalysts were directly synthesized by thermally treating nano-iron oxide powder under different gas atmospheres. The Na_2CO_3-modified catalysts were obtained by mixing the Na_2CO_3 dopant with either FeC_x or FeO_y at varying degrees of intimacy. These pure iron catalysts (FeC_x and FeO_y) and their modified counterparts (Na-FeC_x and Na-FeO_y) were first tested during CO_2 hydrogenation. After subsequent regeneration using syngas (a mixture of CO and H_2), the reactivities of regenerated catalysts were checked and compared with their initial performance to reveal phase-dependent catalytic behaviors. Simultaneously, based on their different reactivity and selectivity toward light olefins, CO, and CH_4, the specific active phases resulting from varying degrees of proximity between iron carbide and Na_2CO_3 were further examined. To further explore the mechanism, the corresponding physicochemical properties of all catalysts were analyzed using ex-situ and in-situ techniques, such as X-ray diffraction (XRD), temperature-programmed oxidation (TPO), X-ray photoelectron spectroscopy (XPS), Mössbauer spectroscopy, and high-resolution transmission electron microscopy (STEM). Using this approach, the active sites of alkali metal-doped iron catalysts responsible for olefin production during CO_2 hydrogenation are systematically revealed and verified experimentally.

2 Materials and methods

2.1 Catalyst Preparation

The pure iron carbide or iron magnetite catalysts were produced by thermal treatment of a commercial nano-Fe_2O_3 powder (NANOCAT, α-Fe_2O_3, 255 m^2*g^{-1}) under different gas atmospheres inside a quartz tubular flow reactor (16 mm diameter, 3 mm wall thickness). Typically, 0.3 g of nano-Fe_2O_3 powder was placed in a boat-shaped crucible and placed into the tube reactor. After purging with an Ar flow (500 Nml/min) for 20 min, the sample was carburized in a syngas atmosphere (3% H_2 and 1.5 % CO in Ar, 500 Nml/min) for 12 h at 300 °C to obtain a batch of pure iron carbide, referred to as FeC_x. After carburization, all carburized samples were in-situ cooled down under a flowing Ar (100 % Ar, 500 Nml/min) atmosphere and then passivated with a diluted O_2 flow (2 % O_2 in Ar, 500 Nml/min) at 25 °C for 2 h to prevent severe oxidation and ignition from direct exposure to air. The pure iron magnetite catalysts were prepared by oxidizing the obtained FeC_x with a steam atmosphere (1% H_2O in Ar, 500 Nml/min) for 12 h at 300 °C, denoted now as FeO_y. When the fresh FeO_y sample was re-carburized again by a syngas atmosphere, the obtained sample

View Article Online
DOI: 10.1039/D6TA00959J

will be named Carb-FeO_y. To compare the effects of water and CO_2 on the oxidation of iron carbide, the same amount of FeC_x sample was treated with a CO_2 (20 % CO_2 in Ar, 500 Nml/min) atmosphere at the same temperature and time, and the resulting sample will be labeled as FeO_z-CO_2. The overall iron-based catalysts preparation procedure is illustrated in Scheme 1. The resulting sample powders were then pressed into pellets, crushed, and sieved to obtain granules in the size range of 250–500 μm.

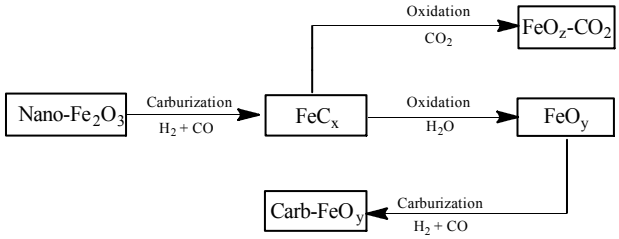

Scheme 1. The pure iron-based catalysts were synthesized by thermally treating nano–iron oxide powder under different gas atmospheres.

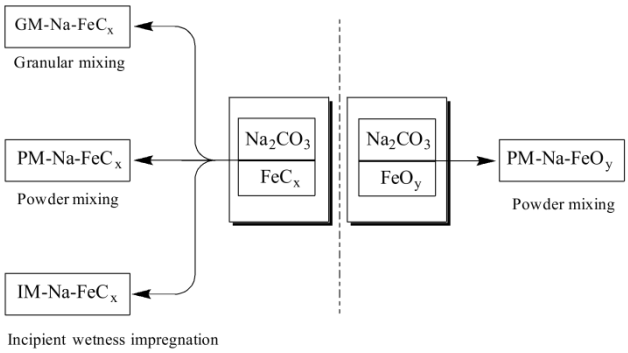

Scheme 2. Na_2CO_3-modified iron catalysts were prepared by mixing the Na_2CO_3 dopant with either FeC_x or FeO_y at varying degrees of proximity.

The Na-modified iron catalysts with different proximities between Na_2CO_3 and pure iron-based catalysts but with the same composition (n_{Fe}: n_{Na} = 1:0.02 molar ratio) were prepared as illustrated in Scheme 2. The PM-Na-FeC_x or PM-Na-FeO_y were prepared by powder mixing (PM) by grinding Na_2CO_3 powder (Sigma Aldrich >99%) with FeC_x or FeO_y powder in a mortar, respectively. The mixtures were then pressed into pellets, crushed, and sieved into granules of 250-500 μm. GM-Na-FeC_x was prepared by granular mixing (GM) of the obtained pure FeC_x granules with Na_2CO_3 particles (250-500 μm). IM-Na-FeC_x was prepared by a single-step incipient wetness impregnation (IWI) of granular FeC_x (250-500 μm) using an aqueous solution of Na_2CO_3 at room temperature. After impregnation, the sample was dried overnight at 110 °C before use.

2.2 Reactor experiments

Catalytic reaction tests were conducted in a stainless-steel fixed-bed reactor (VINCI Technologies) with an inner diameter of 8.3 mm and a length of 215 mm. Typically, 1 g of granular catalyst was packed into the reactor tube and flushed with an Ar flow (100 Nml/min) at 30 °C for 20 min at ambient pressure before the reaction. Then, a feed gas mixture with an H_2/CO_2 ratio of 3 was introduced into the reactor at a gas hourly space velocity (GHSV) of 6000 Nml* g^{-1}* h^{-1}, and the reactor temperature was slowly increased at a ramping rate of 2 °C/min. Afterward, the reactor pressure started to build up until the temperature reached 325 °C. The performance of CO_2 hydrogenation was recorded when the reaction pressure was stable at 20 bar. To keep the reaction products completely in the vapor phase without condensation, the temperature of the pipeline between the reactor and cold trap was maintained at about 200°C during the reaction. All effluent gas passed through a cold trap (25°C) to remove the water vapor and any heavy hydrocarbons from the products. The selectivity for octane (C_8) and other heavier hydrocarbons (C_{8+}) will not be discussed further in this study, because the selectivity for them was found to be less than 1% among all products after an 8 h reaction test. Note proper handling of H_2 is required due to its explosive properties.

The compositions of the gaseous effluents were continuously analyzed by an online gas chromatograph (GC-456, Bruker) equipped with a flame-ionization detector (FID) and a thermal conductivity detector (TCD). The CO_2 conversion and the selectivity for individual hydrocarbon products were calculated according to the equations below [8]. All calculations were performed using data obtained from online GC analysis. Based on the experimental calculations, the carbon balance was maintained within 100 %± 5%. Any deviations beyond the acceptable experimental error range were addressed by repeating the corresponding reaction conditions. The errors of the datasets and the carbon balance calculation results can be found in the online original data repository.

CO conversion:

$$X\_CO_2 = \left(n_{CO_2,\,in} - n_{CO_2,\,out}\right) / n_{CO_2,\,in} \times 100\%$$

CO selectivity:

$$S\_CO = n_{CO} / \left(n_{CO_2,\,in} - n_{CO_2,\,out}\right) \times 100\%$$

C_iH_j selectivity among all products:

$$S\_C_iH_j = i * n_{C_iH_j} / \left(n_{CO_2,\,in} - n_{CO_2,\,out}\right) \times 100\%$$

Where $n_{CO_2,\,in}$ refers refers to the molar flow of CO_2 at the inlet, whereas $n_{CO_2,\,out}$, n_{CO}, $n_{C_iH_j}$ represent the molar flow of the outlet CO_2, CO, and individual hydrocarbons, respectively. The symbol i is the number of carbon atoms in a given hydrocarbon.

Regarding the spent catalyst after reaction, the reaction process leads to partial oxidation of the catalyst and the formation of a surface oxide layer. After 8 h on stream, all spent catalysts were first flushed with an Ar flow (100 Nml/min), then cooled to room temperature before being removed from the steel reactor, and quickly transferred to sealed glass vials.

For catalyst regeneration, the spent catalysts were directly loaded into a quartz tubular reactor, purged with Ar flow again, and subsequently carburized under a syngas atmosphere (3% H_2 and 1.5 % CO in Ar, 500 Nml/min) for 12 h at 300 °C; When regenerated catalysts were subjected to ex situ characterization, a surface passivation treatment was applied

View Article Online
DOI: 10.1039/D5TA00059J

prior to air exposure, using 1% H_2O in Ar at 300 °C for 12 h, as described in the catalyst preparation section. All catalyst (fresh, spent and regenerated) samples were finally stored in a vacuum glass desiccator to minimize exposure to air and moisture and prevent further oxidation. Samples intended for Mössbauer analysis were transported in sealed vials and stored in containers with silica gel desiccant during shipment. Upon opening, all sample handling and storage were conducted in a glove box to minimize exposure to moisture and atmospheric oxygen prior to Mössbauer measurements.

The activity test of the regenerated (or re-carburized) catalyst was conducted using the same procedure as for the fresh catalysts. Here, the names of all spent, regenerated, and spent-regenerated catalyst samples are labeled and distinguished by adding a prefix such as 'Spent-', 'Regen-', or 'Spent-Regen-' to the names of the fresh catalyst samples, respectively.

Transient experiments with different gas hourly space velocities (GHSV) were conducted on catalysts whose phase compositions had reached dynamic equilibrium. Before a given run, the fresh catalyst was first operated at a GHSV of 6000 $Nml*g^{-1}*h^{-1}$ for 8 h to allow the phase composition to reach equilibrium. Then, the catalyst was run sequentially at GHSVs of 1000, 6000, 10000, 6000, and 2000 $Nml*g^{-1}*h^{-1}$ for 1.5 h. Repeated operation at a GHSV of 6000 $Nml*g^{-1}*h^{-1}$ was conducted to examine whether the catalytic performance, related to the phase state, changed after the catalyst had been exposed to low or high space velocities. Other reaction conditions, such as the reaction temperature of 325℃ and the reaction pressure of 20 bar, remained unchanged throughout the experiments.

2.3 Catalyst Characterization.

Ex-situ X-ray diffraction patterns (XRD) of samples were measured under ambient air conditions using a Bruker D8 X-ray diffractometer with a CuKα (λ=1.54Å) radiation source. The diffraction angles (2θ) were scanned from 10 to 80° with a step size of 0.029° and a dwell time of 1 s.

In-situ XRD experiments were conducted using a Rigaku D/max-2600 powder diffractometer (Rigaku, CuKα radiation) equipped with a high-temperature XRK-900 (Anton Paar) sample chamber and a gas supply system for thermal treatment under various atmospheres. All in-situ XRD patterns were recorded in the 2θ scanning range from 10° to 80° using a step size of 0.02° (2θ) and a time per step of 2 s. Typically, the sample powder (~20 mg) was placed into a sample holder, inserted into the chamber, and purged with an Ar flow (20 Nml/min) for 10 min. Subsequently, carburizing gases (3 Nml/min of H_2, 1.5 Nml/min of CO, and 20 Nml/min of Ar), or reactant gases (18 Nml/min of H_2, 6 Nml/min of CO_2) were introduced into the chamber, and XRD patterns were recorded at temperatures ranging from 25℃ to 500 ℃ with dwell periods of 20 min at each target temperature. The ramping rate between the two target temperatures was 5 ℃/min, and all experiments were performed at atmospheric pressure.

The room temperature ^{57}Fe Mössbauer spectroscopic analysis was conducted on an MFD-500AV-02 transmission spectrometer (Topologic Systems). A ^{57}Co (Rh) source in constant acceleration mode was used as the radioactive source. The obtained spectra were analyzed and fitted using the MossWinn program, which modelled the spectra as appropriate superpositions of quadruple doublets and sextets of Lorentzian lines. The components of the iron phase were identified by parameters of the derived spectra, such as the isomer shift (IS), the quadruple splitting (QS), and the magnetic hyperfine field (Hhf). □-Iron foil was used to calibrate the doppler velocities and isomer shift at room temperature.

The X-ray photoelectron spectroscopy (XPS) measurements were performed on a PHI 5000 VersaProbe III scanning XPS microprobe system equipped with a monochromatic Al Kα (hv =1486.6 eV) radiation source. The C1s spectrum with the binding energy of 284.8 eV served as a reference. To prevent oxidation resulting from prolonged exposure to air, samples were prepared in a glove box and quickly transferred to the sample chamber. The pressure within the analysis chamber was maintained below 3×10^{-8} Pa. All samples used for XPS analysis were kept in an argon atmosphere or vacuum throughout the entire transfer process to avoid exposure to air.

The H_2O or CO_2 temperature-programmed oxidation (TPO) experiments were conducted using a flow apparatus comprised of a versatile gas feed system, a quartz tube reactor with an internal necking (L=33cm, Φ4 mm ×2mm), and a mass spectrometer detector (Hiden HPR-20 QUI MS). Typically, the sample was placed in the isothermal zone of the reactor tube and secured by quartz wool plugs. A K-type thermocouple was inserted into the sample bed to monitor and control the temperature during heating. The reactor was surrounded by a metal coil for resistive heating and covered by a layer of quartz wool for thermal insulation. For the H_2O-TPO experiment, 30 mg of granular sample (250 μm -500 μm) was first flushed in an Ar flow for 30 min, and the tube reactor and gas pipelines were preheated to 110 ℃. Afterward, a designed steam flow (2% H_2O in Ar, 100 Nml/min) produced by a water vapor generator was introduced into the reactor until saturation was achieved. The H_2O-TPO was then conducted in a continuous steam flow, with the sample being heated at a ramping rate of 10 °C/min from 110 ℃ to 600 ℃ and held at 600 ℃ for 1 h to ensure complete oxidation. The CO_2-TPO experiment followed a similar temperature ramping procedure as the H_2O-TPO experiment but was conducted in a CO_2 flow (2% CO_2 in Ar, 100 Nml/min). All effluent streams were monitored by an online mass spectrometer, and the signals for H_2O (m/z = 18), CO_2 (m/z = 44), CO (m/z = 28), H_2 (m/z = 2), and CH_4 (m/z =16) were calibrated using a gas mixture of known composition.

The H_2 (or CO)- TPD and H_2-TPR experiments were performed in the same system used in TPO experiments. Before TPD or TPR experiments, 30 mg of power sample (<500 μm) was first carburized at 350 ℃ under a syngas flow (3% H_2 and 1.5 % CO in Ar) for 30 min, followed by flushing with Ar for 30 min while cooling the sample to 50 ℃. For the subsequent TPD experiments, H_2 or CO adsorption (2%CO in Ar, or 2%H_2 in Ar) was carried out at 50℃ for 1h, Finally, desorption was performed under a pure Ar flow with a heating rate of 10 ℃ from 50℃ to 800 ℃, followed by holding at 800 ℃ for 30 min.

View Article Online
DOI: 10.1039/D6TA00959J

The H_2-TPR experiments were conducted using a gas mixture of 5%H_2 in Ar, the reduction temperature was increased from 50 °C to 800 °C at a heating rate of 10 °C, and maintained at 800 °C for 30 min. Note proper handling of H_2 and CO is required due to their respective explosive and toxic properties.

Scanning Transmission Electron Microscopy (STEM) images and HAADF / BF (High Angle Annular Dark Field/Bright Field) STEM images were acquired by using a JEOL JEM ARM200F with a Cs-corrected probe and 200 kV high tension. The incident probe with a nominal 8.7 pA current at a convergence semi-angle of about 20 mrad was used for HAADF and BF images. The acquisition time was set to 10.8 s for a full-size image (4096×4096) to reduce the sample drift for minimizing the image distortion. The elemental mapping was acquired using energy dispersive spectroscopy (EDS, Oxford X-maxN 100TLE) that scanned over the specimen collaborating with the automatic drift correction during the spectrum collection. Before characterization, all samples were dispersed in anhydrous ethanol and then transferred onto a lacey-carbon thin film for the STEM analysis.

3 Results and Discussion

3.1 The physicochemical properties of FeC_x and FeO_y catalysts.

The starting material, fresh nano-sized iron oxide powder (NANOCAT, MACH-1 Inc.), has been widely reported in previous works [20-23]. As a nanosized commercial iron oxide, it consists of poorly crystalline iron oxide (α-Fe_2O_3) with an average particle size of 6.2 nm (Figure S1) and a surface area of 255 m^2/g after drying [23]. Its good availability and high stability ensure its consistency for material pretreatment and modifications in subsequent research. When the nano-sized Fe_2O_3 (Nano-Fe_2O_3) was exposed to the CO_2 hydrogenation atmosphere, it underwent various phase transitions induced by the reactants (CO_2 and H_2) and the products (CO and H_2O). The ex-situ XRD diffraction patterns of Nano-Fe_2O_3 oxide treated with different atmospheres are listed in Figure 1A. After being treated with a mixture of CO and H_2 (1.5% CO + 3% H_2 in Ar) at a low temperature of 300 °C for 12 h, the obtained sample FeC_x showed only obvious diffractions at 2θ of 39.4°, 44.2°, 47.3°, and 50.2°, indicating that the nano-sized Fe_2O_3 was converted into Fe_5C_2 (JCPDS 36-1248) [10-11, 21], and the purity of the obtained iron carbide was greater than 88.7%. The further detailed quantitative analysis is discussed in Section 3.3. Since the FeC_x sample was passivated with a low oxygen concentration (2% O_2 in Ar) at 25 °C after carburization treatment, an oxide layer formed on its surface. The corresponding STEM image (Figure 1B) revealed that the sample FeC_x primarily consisted of nanorod-shaped particles (particle width ≈ 30 nm) with a core-shell structure. The selected area electron diffraction pattern (SAED, inset image in Figure 1B) of the core further indicated a lattice spacing of 0.21 ± 0.05 nm, corresponding to the (510) plane of crystalline Fe_5C_2 [24]. The thin amorphous shell layer (width ≈ 4 ± 1 nm) was identified as iron oxide rather than carbon. A clear interface between the oxide layer and iron carbide can be clearly distinguished by high-angle annular dark-field imaging (HAADF) STEM, as shown in Figure S2. The shell consists of small amorphous iron oxide species (magnetite, blue box), while the core is composed of crystallites of Fe_5C_2 viewed along the [010] zone axis.

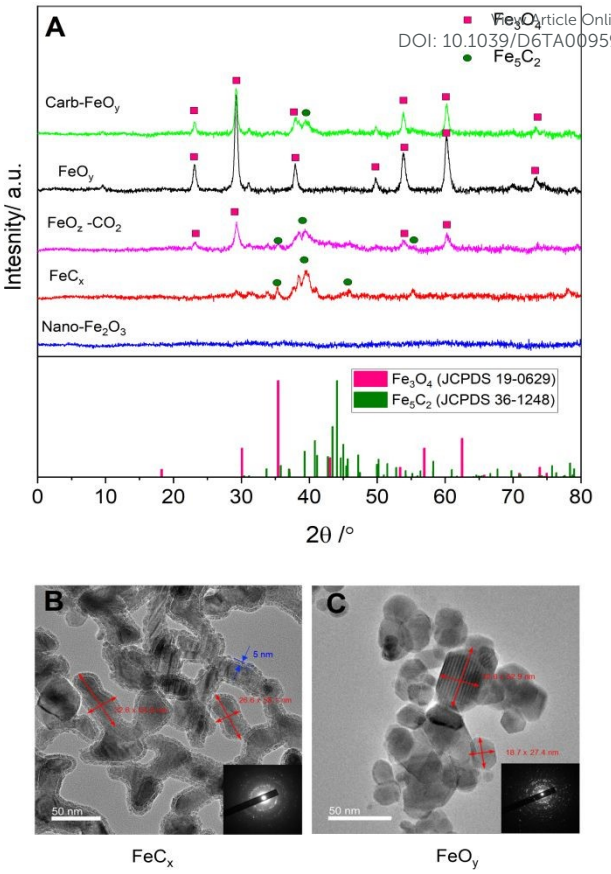

Figure 1. (A) XRD patterns of starting Nano-Fe_2O_3, as-prepared FeC_x, FeO_y catalyst, comparison sample FeO_z-CO_2, and Carb-FeO_y obtained after different gas atmosphere treatments. STEM images of as-prepared FeC_x (B) and FeO_y (C) catalysts. Inset images are selected area electron diffraction patterns (SAED) of the corresponding catalysts.

It has been reported that both CO_2 and H_2O play an important role in oxidizing Fe catalysts during the CO_2 hydrogenation reaction [10]. Here, the ex-situ XRD results further prove that iron carbide is easily oxidized by CO_2 and H_2O, with the oxidation effect of H_2O being significantly stronger than that of CO_2. After being treated with CO_2 (20% CO_2 in Ar) at 300 °C for 12 h, the Fe_5C_2 catalyst was partially oxidized to Fe_3O_4, while a portion of Fe_5C_2 was preserved (Figure 1A). The XRD patterns of the sample FeO_z-CO_2 exhibited both crystalline phases of Fe_3O_4 (JCPDS 19-0629) and Fe_5C_2 (JCPDS 36-1248). In contrast, when the Fe_5C_2 was treated with steam (1% H_2O in Ar) at the same temperature and duration, the iron carbide was completely converted into Fe_3O_4, as indicated by characteristic diffractions at 2θ of 30.1°, 35.4°, 43.2°, 57.1°, and 62.6° (sample FeO_y in Figure 1A), illustrated in Figure 1C. The SAED image (inset in Figure 1C) indicates that the core–shell structure of Fe_5C_2 disappeared and was replaced by even-textured particles. Specifically, clear lattices of crystalline Fe_3O_4 aligned along the

View Article Online
DOI: 10.1039/D6TA00959J

zone axis [110] are observed in the FeO_y sample. The core–shell Fe_5C_2 particles were oxidized into even-textured Fe_3O_4 particles during the steam treatment, providing additional insight into the identification of the shell structure of the iron carbide. In early literature, it was generally speculated that the surface shell of nano-iron carbide particles was decorated by a small amount of Fe_3O_4 or amorphous graphitic carbon [24]. Although it is difficult to completely rule out the presence of graphitic carbon, it is evident that carbon or graphite remains unchanged during the steam treatment. This indirectly confirms that Fe_3O_4, rather than graphitic carbon, is the primary component of the shell structure of the FeC_x sample.

In the following sections, the core–shell structure will be used as a key characteristic to identify the morphology of iron carbide particles. In terms of particle sizes before and after steam treatment, it is worth noting that there was a slight increase in the size of the Fe_3O_4 particles obtained via water treatment of Fe_5C_2. The particles transformed from long, rod-like structures with a rod average diameter of 29 ± 3 nm to irregularly shaped particles with an average diameter of 35 ± 10 nm. When the resulting Fe_3O_4 was subsequently carburized again using CO and H_2 treatment, it was not completely converted back to Fe_5C_2. This is evident in the XRD pattern of the comparison sample Carb-FeO_y (Figure 1A). The partial carburization may be attributed to the growth of the Fe_3O_4 crystals (FeO_y), which likely require higher temperatures for complete carburization than the initial nanocrystals (Nano-Fe_2O_3).

To study the details of the carburization of iron oxides under CO and H_2 atmospheres and explore the differences in the temperatures required for carburizing the iron oxide with different particle sizes, in-situ XRD experiments were carried out, with the results shown in Figures 2A and 2B. From the XRD pattern in Figure 2A, the carburization process of Nano-Fe_2O_3 proceeded through the following stages: Fe_2O_3→ Fe_3O_4→ a mixture of FeO and Fe_5C_2 →Fe_5C_2→a mixture of Fe_5C_2 and Fe_3C. For carburizing at 200 ℃ and below, the nanosized Fe_2O_3 was only reduced to Fe_3O_4. The particle size was approximately 10.8 nm (Figure S3, Table S1), estimated from the half-maximum width of the characteristic diffraction peak. When the temperature reached 250 ℃, Fe_3O_4 began to partially reduce to FeO (JCPDS 77-2355). Simultaneously, the carburization process commenced, and a weak diffraction peak at 44.2°, attributed to Fe_5C_2, appeared in the XRD pattern of the obtained sample. At 300 ℃, the reduction of Fe_3O_4 to FeO weakened, and the carburization of Fe_3O_4 to Fe_5C_2 became dominant. When the temperature increased to 400 ℃, nearly all iron oxides were carburized into Fe_5C_2. However, high-temperature carburization also led to carbon deposition due to the Boudouard reaction, as indicated by a broadened diffraction peak of amorphous carbon at 2θ of approximately 26° in the XRD pattern. It should be noted that, in the experiments to prepare large batches of pure Fe_5C_2 sample (FeC_x), the carburization treatment was carried out at a low temperature of 300 ℃ for 12 h, with small amounts of sample treated per batch. This approach ensured complete carburization while avoiding carbon deposition associated with higher temperatures.

As the reaction temperature continued to increase, the diffraction intensity of both carbon deposits and Fe_5C_2 gradually increased, suggesting that their degree of crystallization also increased, or their particle size grew larger. Furthermore, the diffraction attributed to Fe_3C appeared in the XRD pattern collected at 500 ℃, consistent with previous reports indicating that high temperatures favor the phase transformation from χ-Fe_5C_2 to θ-Fe_3C [14].

Unlike the nanosized Fe_3O_4 (Figure 2A, the sample after 200 ℃ carburization of the Nano-Fe_2O_3), which consisted of small particles (DP ≈ 10.8 nm), the carburization of the FeO_y sample containing larger Fe_3O_4 particles (DP≈ 21.7 nm, obtained from Figure S3, Table S1) occurred at higher temperatures and followed a different phase transformation path. The XRD patterns of the carburized FeO_y samples, collected at various temperatures, are shown in Figure 2B. As the carburization temperature increased, the phase transformation proceeded in the sequence: Fe_3O_4→ a mixture of Fe_5C_2 and Fe_3O_4→ a mixture of Fe_5C_2 and Fe_3C→ a mixture of FeO, Fe_5C_2, and Fe_3C. When the temperature was below 300 ℃, the FeO_y retained the Fe_3O_4 crystalline phase without any noticeable reduction or carburization. At 350 ℃, carburization of Fe_3O_4 to Fe_5C_2 began, as evident by the weakening of Fe_3O_4 diffractions and the emergence of characteristic Fe_5C_2 diffraction peaks. At 400 ℃ and above, diffraction peaks corresponding to Fe_3C appeared, indicating the phase transformation to Fe_3C. At 500 ℃, the Fe_3O_4 in the FeO_y sample was not fully converted into iron carbide. Instead, the remaining uncarburized iron oxide underwent further reduction to form FeO, and coke formation also began. As a result, the XRD pattern at 500 °C displayed mixed diffraction signals from ferrous oxide (FeO), iron carbide (Fe_5C_2 / Fe_3C), and amorphous carbon (2θ of 26°).

Figures 2C and 2D show the in-situ XRD diffraction patterns of FeC_x and FeO_y samples, respectively, collected in a reaction atmosphere at atmospheric pressure but at different temperatures. These patterns reveal the stability of the two catalysts before the CO_2 hydrogenation reaction begins. The iron carbide catalyst FeC_x remained stable at temperatures below 400 ℃ when exposed to a reactant atmosphere of 25% CO_2 and 75% H_2. Only distinct diffraction peaks attributed to Fe_5C_2 were present in the XRD pattern (Figure 2C). When the temperature exceeded 400℃, a broadened diffraction peak attributed to amorphous carbon (2θ of 26°) also appeared, and its intensity increased as the temperature rose. In addition, higher temperatures also promoted the phase transition from Fe_5C_2 to Fe_3C, as indicated by the trace diffraction of Fe_3C in the XRD pattern of FeC_x after treatment at 500 °C. The FeO_y catalyst also exhibited high stability below 400 °C. Under the CO_2 and H_2 atmosphere, the phase transformation of FeO_y occurred only above 500 °C. Unlike the FeC_x catalyst, the FeO_y catalyst underwent reduction and carburization simultaneously during high-temperature treatment, leading to the phase transformation of Fe_3O_4 into iron carbide and ferrous oxide, as illustrated in Figure 2D.

View Article Online
DOI: 10.1039/D5TA09059F

during prolonged exposure to the reactants. Subsequent phase changes of the catalyst are mainly caused by the reaction itself

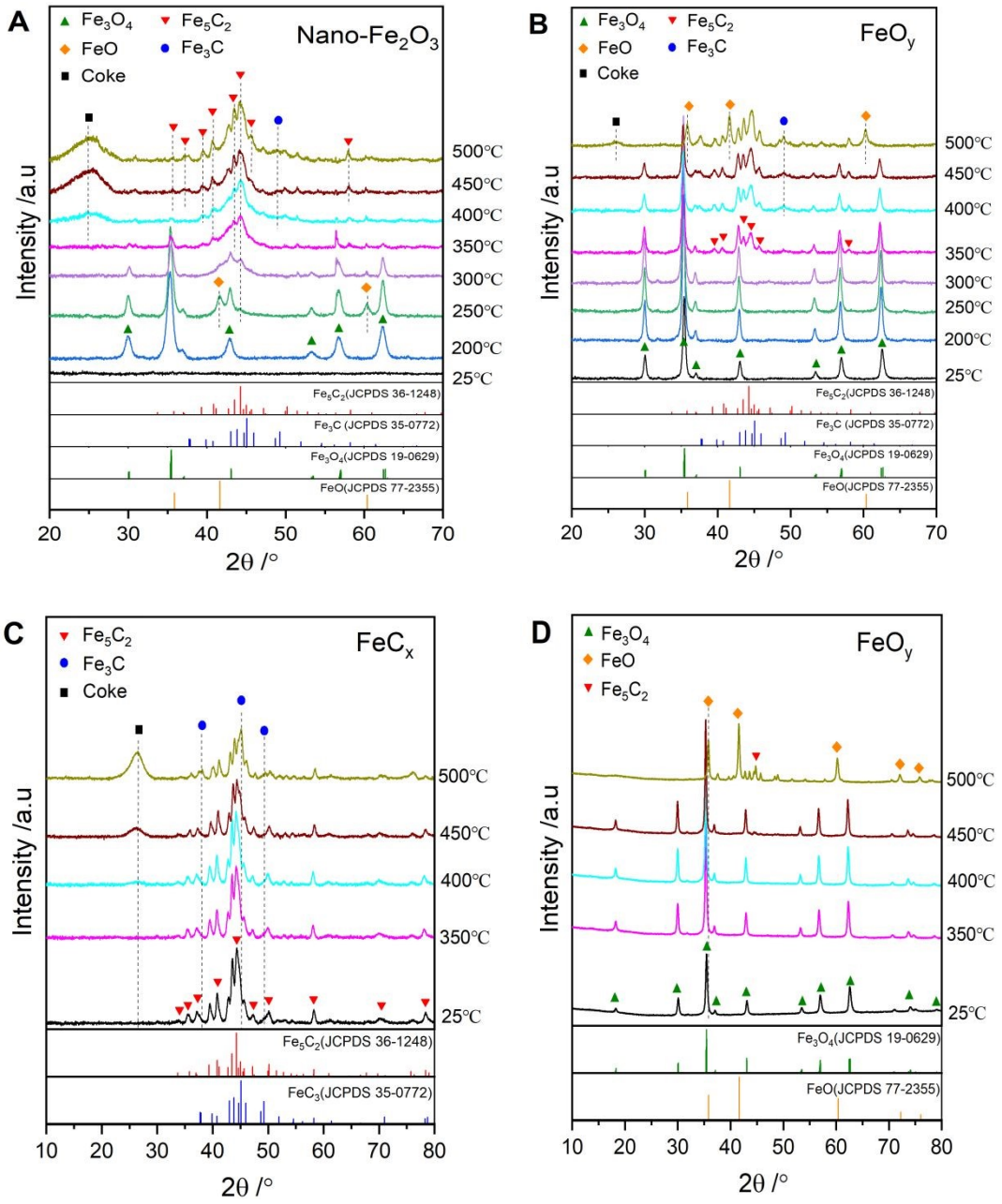

Figure 2. The in-situ XRD patterns of Nano-Fe_2O_3 (A) and FeO_y (B) samples carburized under a syngas atmosphere (3 Nml/min of H_2, 1.5 Nml/min of CO, and 20 Nml/min of Ar), and the in-situ XRD patterns of FeC_x (C) and FeO_y (D) samples treated under a reactant atmosphere (18 Nml/min of H_2, 6 Nml/min of CO_2). The patterns of all samples were collected after stabilization at the corresponding temperatures (25°C, 200°C, 250°C, 300°C, 350°C, 400°C, 450°C, and 500°C) for 20 min.

During CO_2 hydrogenation reaction test in the fixed-bed reactor, the temperature was first increased to 350 °C, followed by a pressure increase to 10 bar to initiate the reaction. The above in-situ XRD results clearly showed that FeC_x and FeO_y catalyst samples were phase-stable in a reactant atmosphere at atmospheric pressure and temperatures below 400 °C. This clears up doubts that the catalyst might undergo phase changes when the reaction pressure increases. Therefore, the bulk phase composition of the fresh catalyst, collected under ex-situ conditions (at room pressure and temperature), can reliably represent the composition of the catalyst just before the reaction begins. It is also reasonable to use ex-situ measurements to study the phase changes of the catalyst during the reaction process.

View Article Online
DOI: 10.1039/D6TA00959J

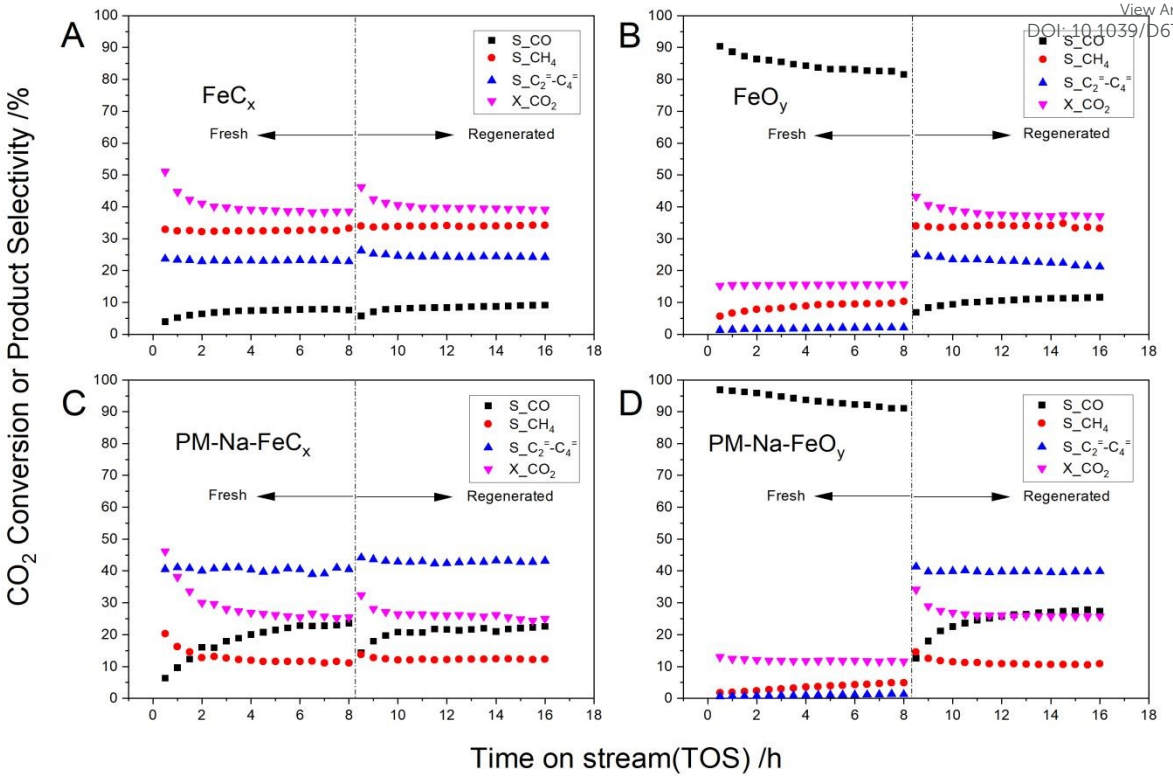

Figure 3. CO_2 hydrogenation performance over fresh & regenerated FeC_x (A), FeO_y (B), PM-Na-FeC_x (C), and PM-Na-FeO_y (D) catalysts. Reaction conditions: Catalyst weight = 1 g, GHSV = 6000 Nml*g^{-1}*h^{-1}, T = 325 ℃, P = 20 bar, H_2/CO_2 = 3 mol/mol.

Up to now, it has been confirmed that the prepared FeC_x catalyst sample is mostly composed of Fe_5C_2 (≥ 88.7%), while FeO_y catalyst sample consists entirely of Fe_3O_4 (comparison in Figures 2A and 2B). FeC_x is synthesized by carburizing nano-Fe_2O_3 at a relatively low temperature of 300 °C and can be oxidized to Fe_3O_4 through water vapor treatment (FeO_y sample). However, even at higher carburization temperatures, FeO_y cannot be fully converted back to Fe_5C_2. This is mainly because the carburization of Fe_3O_4 with different particle sizes follows distinct phase transformation pathways and rates. Since the fresh FeC_x and FeO_y catalyst samples are almost pure phases, similar in particle size, stable before reaction, and capable of undergoing reversible phase transformations under both oxidizing and carburizing conditions, they are used in thus study as model catalysts. All subsequent experiments, results, comparisons, and discussions are based on these model systems.

3.2 Catalytic performance of pure or Na_2CO_3-modified FeC_x and FeO_y catalysts

The catalytic performances of pure and Na_2CO_3-modified FeC_x and FeO_y catalysts are shown in Figure 3 (from A to D). Compared with pure FeO_y (Figure 3 B), the pure FeC_x catalyst (Figure 3 A) exhibited higher Fischer-Tropsch synthesis (FTS) activity with higher CO_2 conversion (X_{CO2} ≥ 40%) and lower CO selectivity (S_{CO} ≤ 10%). In contrast, FeO_y showed higher Reverse Water-Gas Shift (RWGS) activity (S_{CO}≥ 80%, X_{CO2} = 15%). During CO_2 hydrogenation, the fresh FeC_x catalyst was likely oxidized and partially transformed into FeO_y catalyst (Figure 3A), leading to a gradual decrease in the conversion of CO_2 from 51.2 % to 38.9% over 4 h of time on stream (TOS). Concurrently, the selectivity for CO increased from 3.9% to 7.4%, and then reached an approximate steady state. After re-carburizing the spent FeC_x catalyst (TOS = 8 h), the regenerated catalyst (TOS = 8.5 h) exhibited enhanced activity and reduced CO selectivity compared to the spent state (TOS = 8 h). Notably, the steady-state activity of the regenerated catalyst was very similar to that of the fresh catalyst. This indicates that the deactivated FeC_x catalyst can be efficiently restored by re-carburization and confirms that Fe_5C_2, rather than Fe_3O_4, serves as the effective catalytic phase for CO_2 conversion and hydrocarbon formation. This conclusion is further supported by the high activity of the carburized (or regenerated) FeO_y catalyst. After carburization with syngas (as shown in Figure 3B at TOS = 8.5 h), the nearly FTS-inert Fe_3O_4 can be partially converted into active Fe_5C_2, as demonstrated in the previous sections (Figure 1 A, Carb-FeO_y sample). Consequently, the carburized FeO_y catalyst exhibited high FTS activity, comparable to that of the FeC_x catalysts.

High selectivity for light olefins was achieved over a fine physical mixture of FeC_x catalyst and Na_2CO_3 dopant (Figure 3C). In contrast, a similar mixture of FeO_y and Na_2CO_3 was not active for producing light olefins or other hydrocarbons. The performance of PM-Na-FeO_y was almost the same as that of the fresh FeO_y catalyst (Figure 3B and 3D, TOS ≤ 8 h). However, once

View Article Online
DOI: 10.1039/D6TA00959J

the Fe_3O4 within FeO_y was carburized into Fe_5C_2, the mixed catalyst quickly established high activity for CO_2 conversion and high selectivity for light olefins at TOS of 8.5 h (Figure 3D). This fully confirms that the active center for olefin production originates from the combination of Fe_5C_2 and Na_2CO_3. Nevertheless, regardless of Na modification, all catalysts containing Fe_5C_2 experienced initial deactivation at the beginning of the reaction. As the reaction time progressed, CO_2 conversion decreased while CO selectivity increased until a steady-state equilibrium was reached. Notably, the CO selectivity was higher and increased more significantly in the sodium-containing samples than in the sodium-free counterparts. For FeC_x or carburized FeO_y, the CO selectivity remained below 10%, whereas for PM-Na-FeC_x or carburized PM-Na-FeO_y, the CO selectivity reached as high as 25 % at steady-state.

3.3 The phase transition of the pure FeC_x and FeO_y catalysts during CO_2 hydrogenation

Since the combination of iron carbide and sodium is a key active center for olefin production, both sodium-free and sodium-containing catalysts exhibited a similar activity decay trend of first decreasing and then reaching a steady state. However, they were restored to short-term activity after carburization treatment, so it is essential to gain a deeper understanding of phase transitions occurring related to the diverse catalytic performances. First, the phase change-induced deactivation and regeneration (carburization) of the sodium-

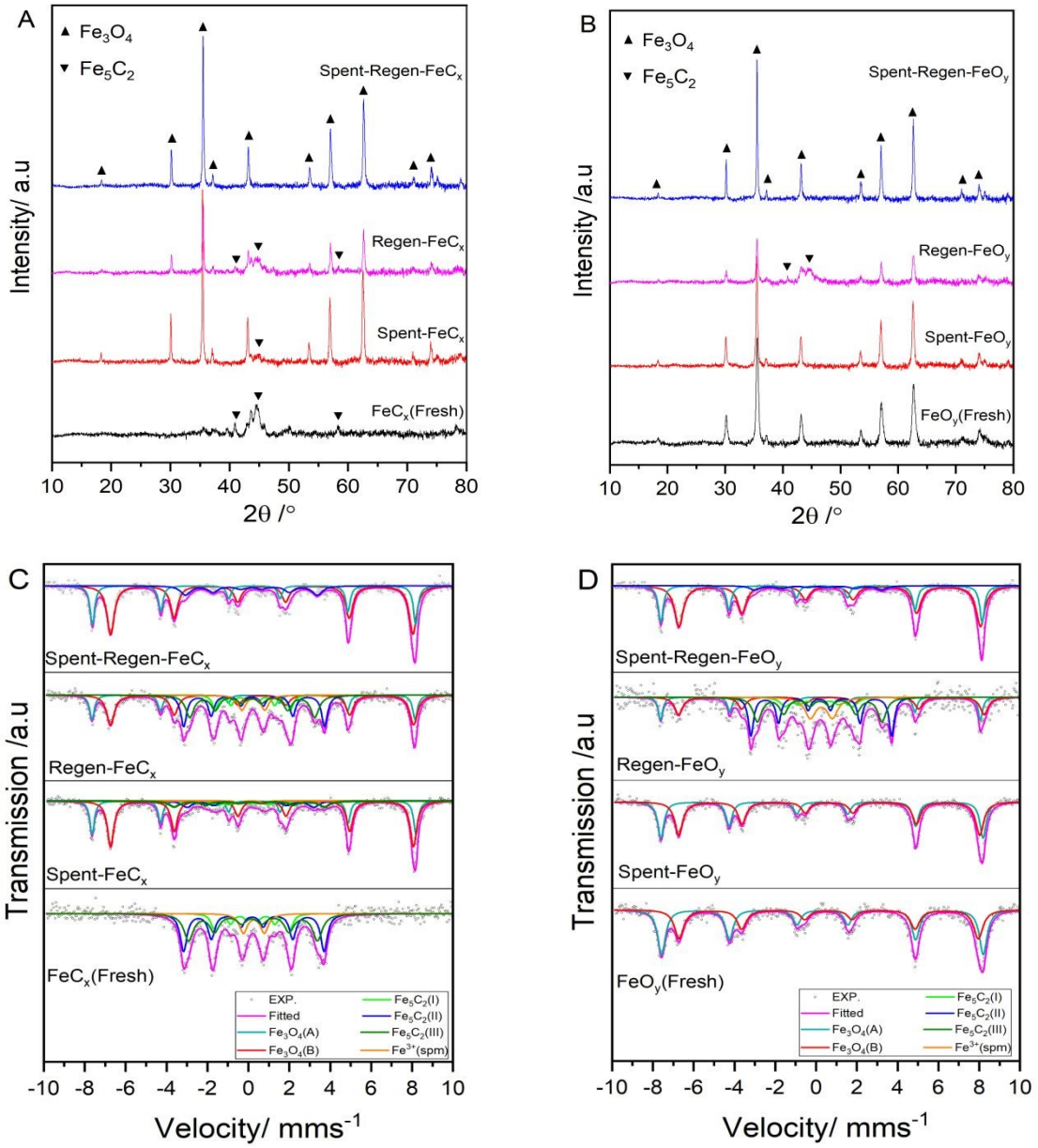

Figure 4. The ex-situ XRD patterns of FeC_x (A) and FeO_y (B) catalysts in fresh, spent, regenerated, and final spent-regenerated states. The corresponding ex-situ Mössbauer spectra of FeC_x (C) and FeO_y (D) catalysts in their corresponding states.

free catalysts were explored using ex-situ XRD, Mössbauer spectroscopy, XPS, and STEM.

For the FeO_y catalyst, after the CO_2 hydrogenation reaction, the bulk phase composition of the spent catalyst remained

View Article Online
DOI: 10.1039/D6TA00950J

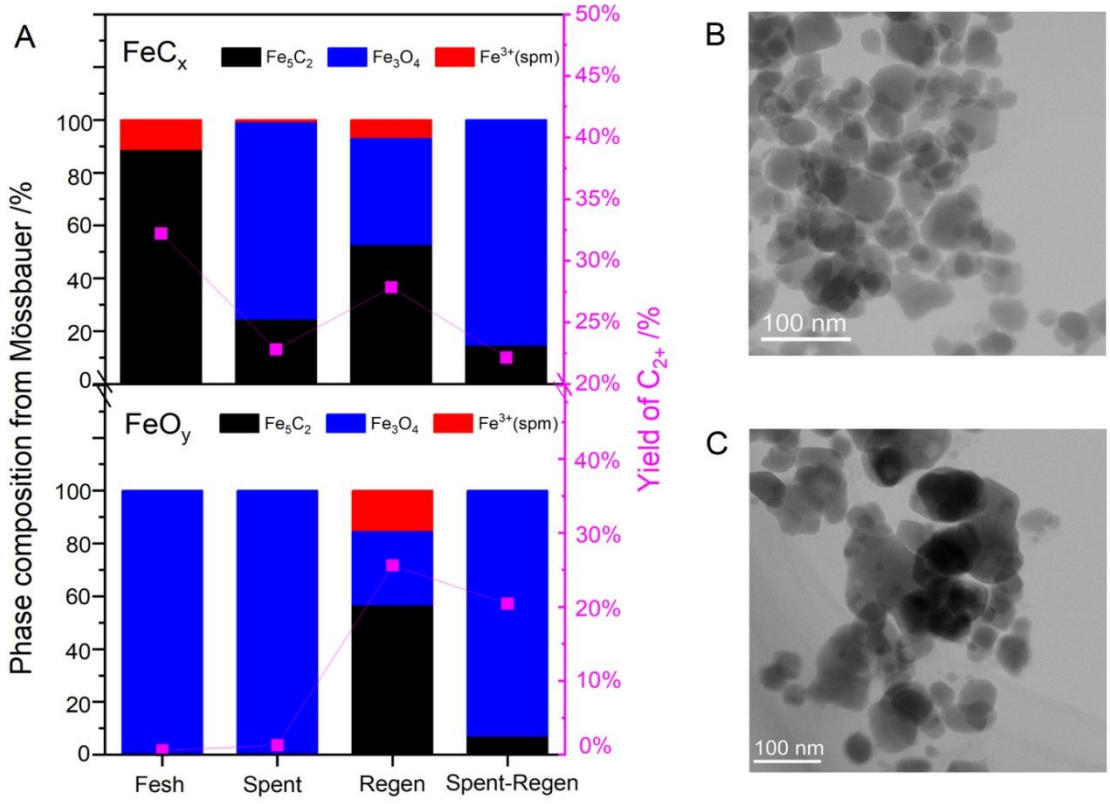

Figure 5. (A) Relationship between the bulk composition from Mössbauer spectroscopy of two iron catalysts and their corresponding C_{2+} yields. (B) STEM image of Spent-FeO_x catalyst, (C) STEM image of Spent-Regen-FeO_y catalyst. The positions of Fe_5C_2 particles are marked with red dashed lines in images, as Fe_5C_2 has typical core-shell structural characteristics. For the definitions in Figure A, Fresh: The fresh FeC_x and FeO_y catalysts respectively; Spent: The catalyst after 8 h of CO_2 hydrogenation conditions (GHSV = 6000 Nml*g^{-1}*h^{-1}, T = 325 ℃, P = 20 bar, H_2/CO_2 = 3 mol/mol); Regen: The catalysts after re-carburizing under a syngas atmosphere (3% H_2 and 1.5 % CO in Ar, 500 Nml/min) for 12 h at 300 ℃; Spent-Regen: The regenerated catalyst after a second 8 h run under CO_2 hydrogenation conditions (GHSV = 6000 Nml*g^{-1}*h^{-1}, T = 325 ℃, P = 20 bar, H_2/CO_2 = 3 mol/mol).

Figure 4A and Figure 4B show the XRD patterns of FeC_x (A) and FeO_y (B) catalysts in their fresh, spent, regenerated (carburized), and final spent-regenerated states, respectively. For the FeC_x catalyst, the fresh state contained only pure Fe_5C_2 iron carbide species. After 8 h of the catalytic reaction, most of the Fe_5C_2 species were oxidized to Fe_3O_4 species. Compared with stable Fe_5C_2 under the reactants' atmosphere (CO_2 + H_2) at 400 °C and atmospheric pressure (Figure 2C), the reactant CO_2 and product H_2O were proven to be direct oxidizing agents that oxidize Fe_5C_2 under high temperature and high-pressure conditions. However, when the spent catalyst was treated with syngas (CO + H_2), part of the Fe_3O_4 species was carburized back into the Fe_5C_2 species. Consequently, the regenerated FeC_x catalyst (Regen-FeC_x) had restored FTS activity, evident by higher CO_2 conversion and increased selectivity for hydrocarbons. After another reaction cycle, nearly all the Fe_5C_2 phase in the regenerated catalyst was oxidized back to the Fe_3O_4 phase. See the XRD pattern of the spent- regenerated FeC_x catalyst (Spent-Regen-FeC_x).

nearly unchanged compared with the fresh one: both exhibited pure Fe_3O_4 phases, which also explained their lower activity during CO_2 hydrogenation. After carburization treatment with syngas, the carburized FeO_y catalyst showed a mixture of crystalline Fe_3O_4 and Fe_5C_2 phases and exhibited good activity similar to the regenerated FeC_x (Regen-FeC_x) catalyst. This suggests that H_2 and CO can be used to form the active Fe_5C_2 phase. Like the regenerated FeC_x catalyst, the carburized FeO_y catalyst was also unstable. After an additional 8 h of CO_2 hydrogenation, the most of Fe_5C_2 phase were oxidized, and the XRD patterns of the spent-regenerated FeO_y catalyst (Spent-Regen-FeO_y) showed predominantly Fe_3O_4 crystal phases.

Further quantitative and qualitative analysis of the bulk phase composition of the catalysts at different states (fresh, spent, regenerated, and final spent-regenerated) was performed using Mössbauer spectrometry (MES), and the results are shown in Figures 4C and 4D. The detailed parameters are listed in Tables S2 and S3. The sextets with Hhf of around 491 ± 1 and 460 ± 5 kOe are commonly attributed to the tetrahedral (A) and octahedral (B) sites of Fe_3O_4, respectively [13, 25-27]. The sextets

View Article Online
DOI: 10.1039/D6TA00951J

with Hhf of 116 ± 3, 213 ± 2, and 190 ± 5 kOe are assigned to the three different nonequivalent sites of Fe_5C_2 [13, 26, 28]. Another observed doublet is likely ascribed to the superparamagnetic phase (spm) of Fe^{3+} [13] or FeO [29]. The quantitative analysis from MES was consistent with the XRD results. The fresh FeC_x catalyst exhibited an almost entirely Fe_5C_2 (≥ 88.7%) bulk composition, while the fresh FeO_y catalyst consisted purely of Fe_3O_4 species (100%). After the CO_2 hydrogenation, 74.8% of the Fe_5C_2 species in the FeC_x catalyst were oxidized to Fe_3O_4 species, while the pure FeO_y catalyst (formed via H_2O treatment of FeC_x) had a stable phase composition, with 100% Fe_3O_4 content both before and after reaction. Upon carburization of the spent catalysts with syngas, more than 50% of the iron carbide components were restored in the regenerated catalysts. The Fe_5C_2 contents in the regenerated FeC_x (Regen-FeC_x) catalyst and carburized FeO_y catalyst (Regen-FeO_y) are 52.8% and 56.6%, respectively. However, continued reaction once again oxidized iron carbide to iron oxide. The residual Fe_5C_2 content in the spent-regenerated FeC_x (Spent-Regen-FeC_x) and spent-regenerated FeO_y (Spent-Regen-FeO_y) catalysts decreased to 14.7% and 7.1%, respectively.

The bulk composition of FeC_x and FeO_y catalysts was correlated with their corresponding FTS activity (represented by the yield of C_{2+}) at different stages, as shown in Figure 5A. The results indicated that Fe_5C_2 was the active phase responsible for hydrocarbon production during CO_2 hydrogenation. Notably, regardless of whether the Fe_5C_2 phase originated from carburized nano-Fe_2O_3 (in FeC_x series) or was formed by carburizing bulk Fe_3O_4 (in FeO_y series), only a small amount (≤ 30%) of active Fe_5C_2 phase could be preserved, eventually reaching a dynamically stable state during the CO_2 hydrogenation reaction.

For example, the fresh FeC_x catalyst contained 89% Fe_5C_2 and yielded 32% C_{2+} products. In contrast, the Spent-FeC_x catalyst, with only 25% Fe_5C_2 remaining, showed a reduced C_{2+} yield of 23%. Interestingly, the Spent-Regen-FeO_y catalyst, despite having just 7.1% Fe_5C_2, still achieved a C_{2+} yield of 20%. This raises the question: why were these catalysts, containing relatively small amounts of Fe_5C_2 phase, still highly FTS-reactive even though their XRD diffractions looked indistinguishable from pure Fe_3O_4? To ascertain the reason for this apparent discrepancy, the detailed morphologies of the inactive Spent-FeO_y and active Spent-Regen-FeO_y catalysts were studied and compared, as shown in Figures 5B and 5C, respectively. The Spent-FeO_y catalyst contained only even-textured particles with an average particle size of 64 nm. Combining the results of XRD and Mössbauer spectroscopy analysis, these particles were identified as Fe_3O_4. In contrast, the Spent-Regen-FeO_y catalyst contained both even-textured particles (~89 nm in average) and smaller particles (~40 nm) exhibiting a core-shell structure. In particular, the number of core-shell particles was less than that of the even-textured particles in the mapping area. As discussed previously, the core-shell structure was the special characteristic of iron carbide species, whose surface has always been oxidized into Fe_3O_4 during the passivation treatment or exposed to air during sampling.

In the Spent-Regen-FeO_y catalyst, further EDX analysis of selected regions around the core–shell particles clearly distinguished the boundary between iron carbide and iron oxide, indicating that these core-shell particles consist of iron carbide in cores surrounded by iron oxide surface layers. The other even-textured particles were identified as iron oxides. Combining these observations with XRD and Mössbauer spectra results, it can be further concluded that these iron carbides were Fe_5C_2, and iron oxides were Fe_3O_4. Additionally, the formation of larger Fe_3O_4 particles in the Spent-Regen-FeO_y catalyst may be attributed to particle aggregation during the reaction. XRD results also confirmed this sintering behavior, as evidenced by the larger size of Fe_3O_4 crystals in the Spent-Regen-FeO_y catalyst compared to those in the Spent-FeO_y catalyst (Figure 4B, Table S1).

XPS analysis further revealed differences in the surface iron species between the Spent-FeO_y and Spent-Regen-FeO_y catalysts, helping to explain the observed differences in FTS catalytic activity. As shown in Figure S5, the Fe $2p_{3/2}$ peaks centered around 710.7 eV and the Fe $2p_{1/2}$ peaks located around 723.8 eV are attributed to the overlapping signals of Fe^{2+}/Fe^{3+} oxide species; The binding energy of Fe 2p peaks of Fe atoms in Fe-C structures are located at 706.7 eV (Fe $2p_{3/2}$) and 719.9 eV (Fe $2p_{1/2}$) [26]. It is evident that the surface species of the fresh and reacted FeO_y catalysts were predominantly iron oxide species. However, after the carburization treatment with syngas, iron carbide species began to form on the surface of Regen-FeO_y. The Spent-Regen-FeO_y catalyst still retained iron carbide on its surface after CO_2 hydrogenation, although its content had decreased significantly, as indicated by the weakening of the Fe–C related Fe 2p peaks in Figure S5. Interestingly, although the Fe_5C_2 content in the bulk phase of the Spent-Regen-FeO_y catalyst was six times lower than that of the Regen-FeO_y catalyst according to quantitative Mössbauer spectroscopy analysis, the difference in surface iron carbide content is small. This may suggest that Fe_5C_2 was enriched on the surface of the Spent-Regen-FeO_y catalyst, thereby contributing to its observed reactivity. Overall, the small size of the iron carbide particles and their higher surface concentration likely explain why the Spent-Regen-FeO_y catalyst maintains considerable activity despite the low iron carbide content in its bulk phase.

Notably, the particle size of surface iron carbide is also closely related to the catalytic performance [10,17]. From the discussion in **Section 3.1**, it was shown that small particles of Fe_3O_4 and Fe_5C_2 can transform into each other under different $CO+H_2/CO_2$ (H_2O) atmospheres. However, once the particles grew larger, the phase transformation became less reversible at low temperatures (≤ 350 °C). In the early stages of the reaction, catalysts containing a large number of smaller Fe_5C_2 particles exhibited higher CO_2 conversion activity. However, the water produced by the reaction accelerated the oxidation of Fe_5C_2 into less-active Fe_3O_4, and the hydrothermal atmosphere also promoted particle growth, leading to a gradual decline in activity. At the same time, the increasing iron oxide content and decreasing iron carbide content resulted in enhanced CO selectivity. As the reaction proceeded, the increased CO production carburized only the small Fe_3O_4 particles, while the larger Fe_3O_4 particles remained unconverted. Therefore, in Fe_5C_2-containing catalysts, after the initial decline in activity, the reaction tended to reach a steady-state activity. This behavior was mainly

attributed to the establishment of a dynamic phase equilibrium of Fe_5C_2 within the catalyst, characterized by stable content and particle size.

catalyst produced by mortar grinding and mixing (Figure 6B). The selectivity for light olefins exceeded 40%, but the initial activity (CO_2 conversion) dropped sharply from 46% to 25% and required approximately 8 h to reach a steady state. Further increasing the

View Article Online DOI: 10.1039/D5TA00959J

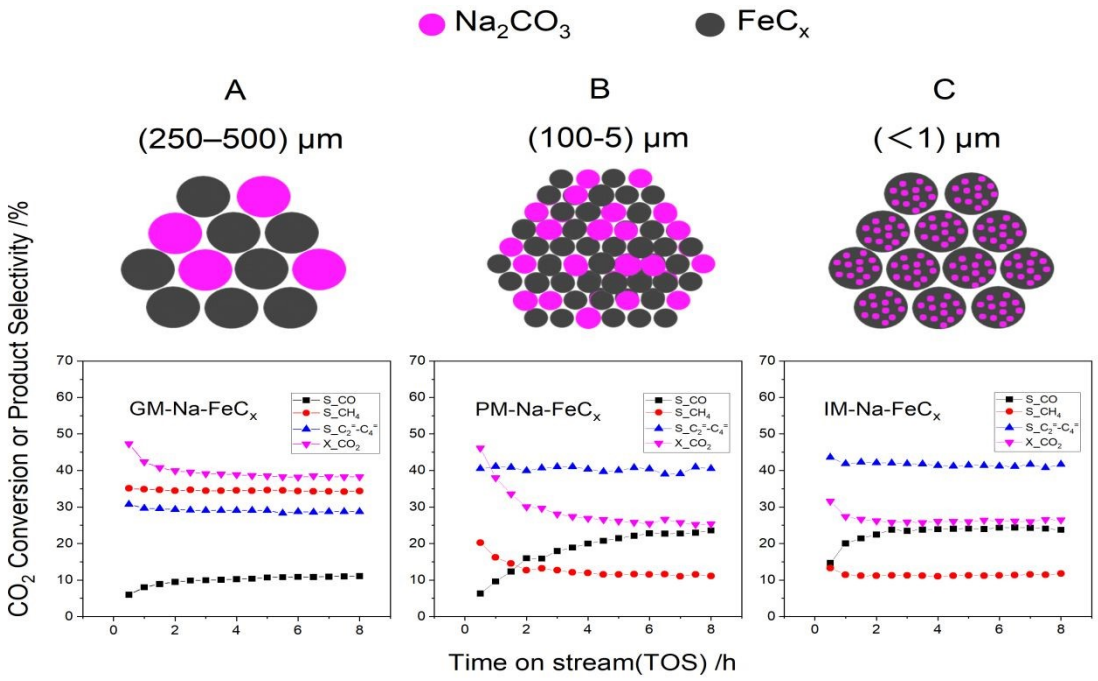

Figure 6.CO_2 hydrogenation over Na_2CO_3-modified FeC_x catalyst with varying initial proximities. (A) Mixing pure FeC_x granules with Na_2CO_3 particles (250 μm -500 μm) in a vial. (B) Mixing FeC_x powder with Na_2CO_3 powder using mortar grinding. (C) Wetness impregnation (WI) of granular FeC_x (250-500 μm) with Na_2CO_3 aqueous solution. The schematic diagram is shown above, and the images below depict the respective catalytic activities. The pink balls represent Na_2CO_3, and the black ones represent FeC_x. Reaction conditions: Catalyst weight = 1 g, GHSV = 6000 NmI*g^{-1}*h^{-1}, T = 325 °C, P = 20 bar, H_2/CO_2 = 3 mol/mol.

3.4 Influence of contact intimacy between Na_2CO_3 and Fe_5C_2 on olefin yield

In previous literature, Fe-based catalysts are typically impregnated with Na or K dopants and then calcined, reduced at high temperatures, or carburized to form effective catalysts for the hydrogenation of CO_2 to produce olefins [9,12-19]. As shown in Figure 3D, the olefin selectivity of the catalyst can be significantly improved by simple physical mixing of Na_2CO_3 and Fe_5C_2 components. To further investigate the interaction between Fe_5C_2 and Na_2CO_3 and to identify the active center responsible for olefin production, three catalysts with identical Na_2CO_3 loadings but different contact distances between FeC_x and Na_2CO_3 were prepared using three different methods. The preparation methods and corresponding catalytic performance are illustrated in Figure 6.

For the GM-Na-FeC_x catalyst (Figure 6A), where the Na_2CO_3 and FeC_x were integrated by granule mixing with a particle size ranging from 250 to 500 μm, its catalytic performance was nearly the same as that of pure FeC_x. Under steady-state conditions, the CO_2 conversion was approximately 38%, and the selectivities for CH_4, light olefins, and CO were 34%, 28%, and 11%, respectively. When the contact distance between Fe_5C_2 and Na_2CO_3 was reduced to 100 - 5 μm, the active centers for olefin production were generated, but the activity was unstable, as demonstrated by the PM-Na-FeC_x proximity between Na_2CO_3 and Fe_5C_2 can rapidly promote the formation of stable active centers for olefin production. The IM-Na-FeC_x catalyst, prepared via incipient wetness impregnation to achieve close contact between the components, exhibited stable performance after 3 h (Figure 6C). Interestingly, when steady-state conditions were reached, the performance of the IM-Na-FeC_x and PM-Na-FeC_x catalysts was very similar. Their CO_2 conversion decreased to 26%, and the selectivity for CH_4 dropped to 11%, while the selectivity for light olefins and CO increased to 40% and 26%, respectively. These results demonstrate that a highly intimate contact between Na_2CO_3 and Fe_5C_2 forms highly active centers to produce light olefins. Similar phenomena have been reported for Fe/C catalysts modified with carbonaceous potassium promoters, in which an appropriate proximity between the potassium species and Fe/C was found to promote the formation of iron carbide, leading to enhanced olefin selectivity and yield [9]. Our findings further confirm that the interface between iron carbide and Na or K carbonate is the key factor in generating highly active sites for olefin production (Figure S6).

The formation and evolution of the active Na_2CO_3-Fe_5C_2 interface within the PM-Na-FeO_y catalysts were visualized using STEM and EDX, as shown in Figure 7, Figures S7, and S8. Before carburization, both the fresh and spent PM-Na-FeO_y catalysts contained only Fe_3O_4

View Article Online
DOI: 10.1039/D6TA00959J

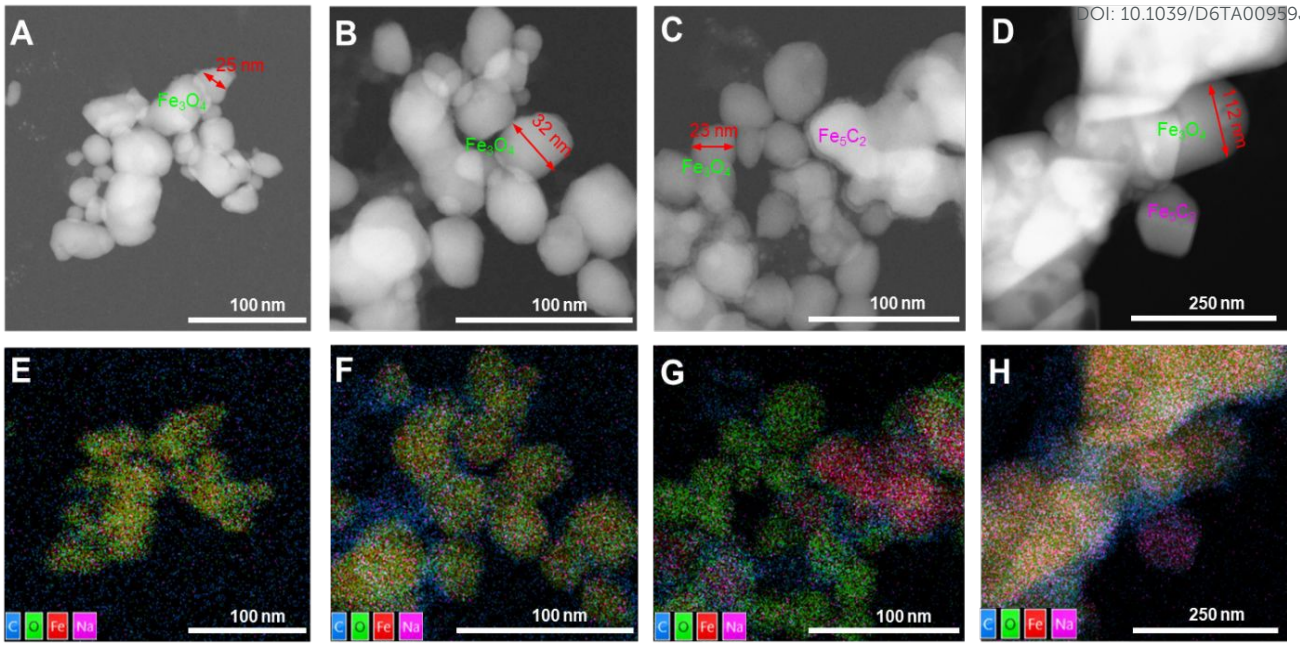

Figure 7. STEM images and corresponding EDX elemental mapping of PM-Na-FeO_y catalyst in fresh (A, E), spent (B, F), regenerated (C, G), and final spent-regenerated (D, H) states.

particles with an average particle size of approximately 30 nm, on which the Na dopants were well dispersed, as seen in Figures 7A, 7B, and the corresponding elemental mapping images (Figures 7E and 7F). After syngas carburization and subsequent oxygen passivation, some Fe_3O_4 particles in the spent PM-Na-FeO_y catalyst were converted into Fe_5C_2 particles, these Fe_5C_2 particles were intermixed with the remaining Fe_3O_4 particles, as shown in the images of the regenerated PM-Na-FeO_y catalyst (Figures 7C and 7G). After 8 hours of the CO_2 hydrogenation reaction again, the morphology of spent-regenerated PM-Na-FeO_y was examined. It was observed that most of the Fe_5C_2 in the catalyst had been re-oxidized, with only a small amount of Fe_5C_2 remaining. In addition, the particle size increased, as shown in Figures 7D and 7H.

The difference between iron carbide (Fe_5C_2) and iron oxide (Fe_3O_4) can be clearly distinguished by the distribution of carbon (C) and oxygen (O) elements in the EDX mapping images (Figures S7 and S8). The C element was more concentrated in the iron carbide regions, while the O element was enriched in the iron oxide regions. Accordingly, in Figure 7, the EDX images show that the Fe_3O_4 particles appeared yellow-green, reflecting enrichment with oxygen (green) and iron (red), whereas the areas containing Fe_5C_2 particles appeared red-pink, indicating enrichment with carbon (blue) and iron (red). In Figures S7 and S8, The Na element is evenly dispersed over both single particles of Fe_3O_4 (Figure S7) and Fe_5C_2 (Figure S8), showing no preferential distribution. During sample preparation for the TEM experiments, the fresh bulk catalyst was ground again and dispersed onto a carbon mesh using anhydrous ethanol as the solvent. As a result, the Na was also evenly distributed at the nanometer scale on the catalysts, which represents a stable state of Na distribution.

Notably, while the fresh and spent PM-Na-FeO_y catalysts contained only interfaces between Fe_3O_4 and Na, the Regen-PM-Na-FeO_y catalyst generated new interfaces between Fe_5C_2 and Na. This is the primary reason for the high yield of light olefins observed in the Regen-PM-Na-FeO_y catalyst. After an additional 8 hours of CO_2 hydrogenation, Fe_3O_4 once again became the dominant phase in the Spent-Regen-PM-Na-FeO_y catalyst (final spent state, see Figure 7). However, a small amount of residual Fe_5C_2 and the corresponding Na–Fe_5C_2 interfaces persisted, as confirmed by the TEM and EDX images in Figure S8. This retention helps explain the Spent-Regen-PM-Na-FeO_y catalyst's ability to maintain a certain level of reactivity. Although its reactivity was lower than that of the Regen-PM-Na-FeO_y catalyst, it remained higher than that of the fresh and spent PM-Na-FeO_y catalysts, which contained only Na–Fe_3O_4 interfaces.

3. 5 Effect of Na_2CO_3 on the phase transition of Fe_5C_2 during CO_2 hydrogenation.

As established earlier, the interface between Fe_5C_2 and Na_2CO_3 serves as the active center to produce light olefins. However, Fe_5C_2 was easily oxidized during the CO_2 hydrogenation reaction, resulting in a decrease in Fe_5C_2 and an increase in Fe_3O_4 content, which in turn results in reduced catalyst activity. To investigate the effect of Na_2CO_3 on the oxidation of Fe_5C_2 species and to explore the reasons behind the lower activity (or CO_2 conversion) and higher CO selectivity observed in sodium-modified catalysts, comparative experiments were conducted between pure FeC_x and Na-modified PM-Na-FeC_x catalysts.

Figure 8A displays the XRD patterns of these two catalysts before and after the reaction. In the fresh PM-Na-FeC_x catalyst, the Na_2CO_3 dopant was evenly dispersed, and no diffraction peaks attributable to sodium carbonate were observed; only diffraction peaks of pure Fe_5C_2 appeared. Moreover, the addition of Na_2CO_3 did not change

View Article Online
DOI: 10.1039/D6TA00959J

the hyperfine interactions of the iron nuclei with their surroundings, as evident from the Mössbauer spectrum of the fresh PM-Na-FeC_x catalyst. These spectra were identical to those of the fresh FeC_x, indicating a high Fe_5C_2 composition (88.8%) as shown in Figure 8B.

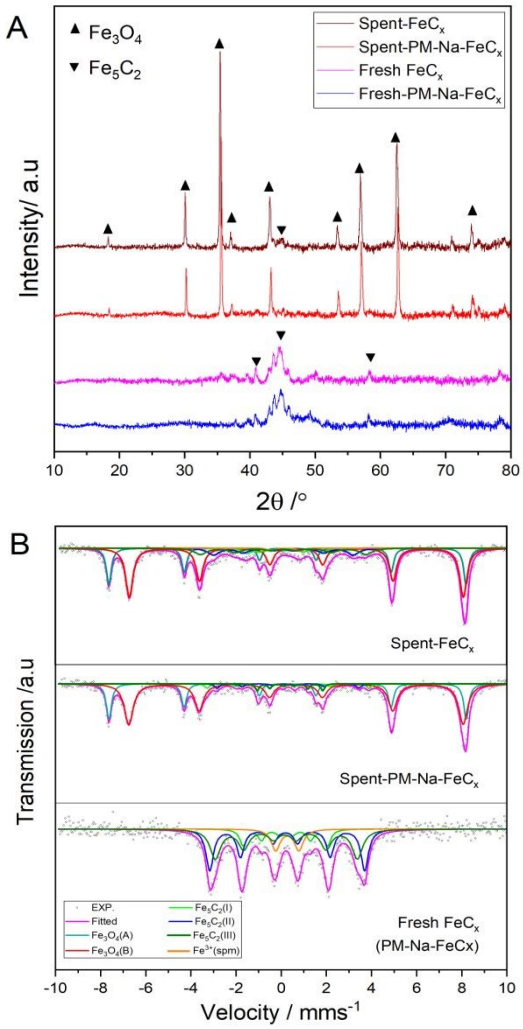

Figure 8. The ex-situ XRD patterns (A) and the corresponding Mössbauer spectra (B) of FeC_x and PM-Na-FeC_x catalysts in fresh and spent states.

After the CO_2 hydrogenation reaction, both the Na-containing and non-Na-containing catalysts underwent oxidation, with most of the Fe_5C_2 transforming into Fe_3O_4. The XRD pattern of Spent-FeC_x exhibited a mixture of diffraction patterns of the remaining Fe_5C_2 and oxidized Fe_3O_4 species, while the XRD pattern of the spent PM-Na-FeC_x catalyst showed only Fe_3O_4 diffraction peaks. Based on the integration of their Mössbauer spectra (Figure 8B), the quantification result indicated that the Fe_5C_2 content in spent PM-Na-FeC_x (11.75%) was lower than that in the spent FeC_x (24.57%), as shown in Table S4. This suggests that Na did not prevent the oxidation of the nanosized Fe_5C_2; rather, the Na-modified nanosized Fe_5C_2 catalyst appeared to oxidize more extensively than the pure Fe_5C_2 catalyst.

The promoting effect of Na_2CO_3 on the oxidation of Fe_5C_2 can be further verified by H_2O-TPO and CO_2-TPO experiments. During the CO_2 hydrogenation, both the reactant CO_2 and product H_2O can oxidize the iron carbide as follows [30]:

$$3FeC_x + (4+3x)H_2O \rightarrow 3xCO + Fe_3O_4 + (4+3x)H_2$$

$$3FeC_x + (4+3x)CO_2 \rightarrow (4+6x)CO + Fe_3O_4$$

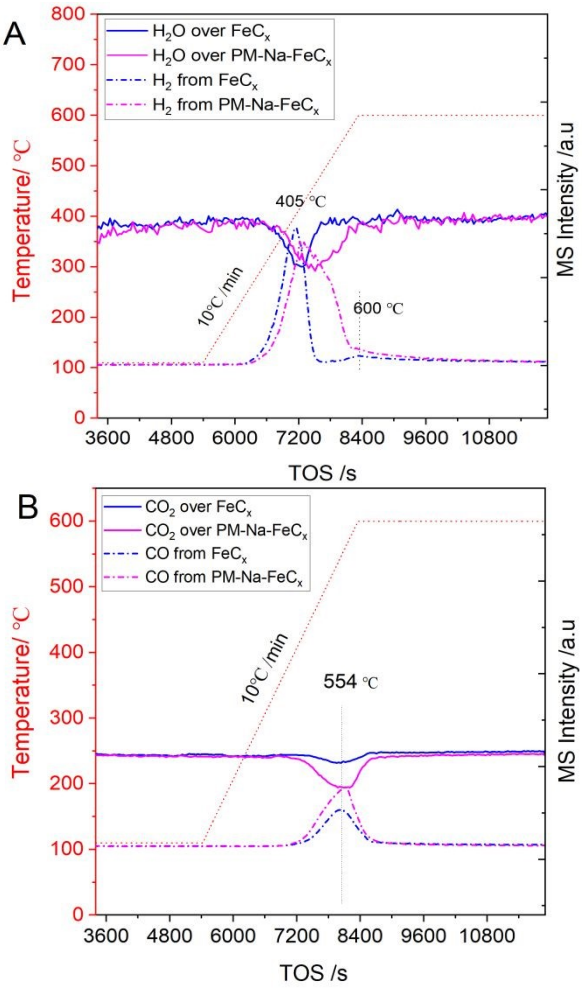

Figure 9. The H_2O-TPO (A) and CO_2-TPO (B) profiles of FeC_x and PM-Na-FeC_x catalysts.

To simulate the oxidation of catalysts during the reaction and investigate the effect of Na_2CO_3 on the oxidation of iron carbide, temperature programmed oxidation (TPO) experiments with FeC_x and PM-Na-FeC_x catalysts were conducted in water vapor and CO_2 atmospheres, respectively. The consumed oxidant and released products were recorded and are shown in Figure 9 and Figure S9. In the H_2O-TPO process (Figure 9A), the oxidation of FeC_x occurred between 250 °C and 460 °C, with a maximum at 405 °C, while the oxidation temperature range of PM-Na-FeC_x was broader, extending from 250°C to 600°C. By examining the amount of consumed water and produced hydrogen, it is evident that the PM-Na-FeC_x catalyst underwent deeper oxidation than the FeC_x catalyst, consuming more H_2O and producing more H_2 effluent. Similar results were observed in the CO_2-TPO experiment (Figure 9B). The PM-Na-FeC_x catalyst exhibited greater CO_2 consumption and lower CO production than the FeC_x catalyst. Additionally, the CO_2 oxidation of FeC_x primarily occurred around 554°C, which is higher than the oxidation temperature of FeC_x in H_2O. This explains why H_2O oxidized iron carbide more completely than CO_2 at lower temperatures (such as

View Article Online
DOI: 10.1039/D6TA00959J

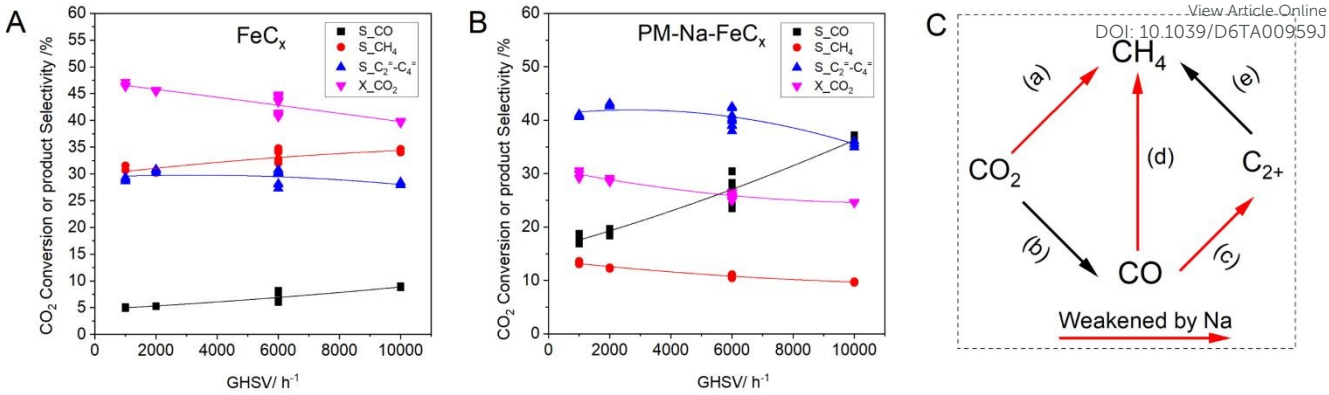

Figure 10 The reactivity of the steady-state FeC_x (A) and PM-Na-FeC_x (B) catalysts with varying gas hourly space velocities (GHSV), and the proposed schemes for product formation during CO_2 hydrogenation (C). Other reaction conditions: Catalyst weight = 1 g, T = 325 °C, P = 20 bar, H_2/CO_2 = 3 mol/mol. The steady-state catalyst refers to a catalyst whose phase content reaches dynamic equilibrium. Usually, the catalyst was first operated at a GHSV of 6000 Nml*g^{-1}*h^{-1} for 8 h to allow the phase equilibrium state to be reached.

300°C), as discussed in **Section 3.1**. Although high-pressure TPO experiments were not conducted, it is reasonable to speculate that the oxidation of iron carbide by H_2O and CO_2 may be more serious under high pressure than under normal pressure. However, our results can be used to explain the different degrees of oxidation for the two catalysts before and after the CO_2 hydrogenation. Compared with the pure iron carbide (FeC_x) catalyst, the sodium-modified iron carbide catalyst (PM-Na-FeC_x) retained less iron carbide after the CO_2 hydrogenation reaction. This is mainly because the Na additive promoted the oxidation of nanosized iron carbide by the product water and the reactant CO_2 during the CO_2 hydrogenation reaction, which is also consistent with the results from XRD and Mössbauer spectroscopy.

3. 6 Steady-state reactivity of phase equilibrated catalysts with and without Na_2CO_3 dopants

In addition to affecting the phase transition of iron catalysts, sodium and other alkali metal dopants are often considered to influence the adsorption and dissociation of hydrogen on the surface of iron catalysts [31-32], and Our H_2-TPD, CO-TPD and H_2-TPR experiments further support this conclusion (Figures S10 and S11). To gain a deeper understanding of the effect of the Na_2CO_3 promoter on product distribution and related kinetics, a series of transient experiments with varying gas hourly space velocities (GHSV) were conducted over the catalysts. The phase transitions of the iron species were assumed to reach a pseudo-dynamic equilibrium once stable catalytic performance was achieved at each GHSV. The resulting reactivity and selectivity for the main products at steady state are presented in Figures 10A and 10B.

Over the FeC_x catalyst, as the GHSV increased, the conversion of CO_2 decreased, while the selectivity for CH_4 and CO increased linearly (Figure 10A), even under extremely high GHSV conditions. This suggests that both the reverse water-gas shift (RWGS) reaction and the CO_2 to methane reaction were initial reactions over FeC_x during CO_2 hydrogenation. Unlike FeC_x catalysts, when the FeC_x catalyst was modified by Na_2CO_3 dopant, its selectivity for CH_4 decreased significantly. As the GHSV increased over the PM-Na-FeC_x catalyst, the selectivity for CH_4 further reduced, while the selectivity for CO increased rapidly, making CO the dominant product (Figure 10B). This indicated that the Na_2CO_3 promoter inhibits the direct hydrogenation of CO_2 to CH_4 over the Na-modified iron catalyst. Moreover, it has been generally accepted that the formation of C_{2+} compounds occurs via the CO-FTS pathway with CO as an intermediate [10, 14, 16]. This was also confirmed by low space velocity experiments on the PM-Na-FeC_x catalyst. As the residence time increased (GHSV decreased), the CO was further converted to C_{2+} hydrocarbons. Therefore, the selectivity of CO decreased, and the selectivity for light olefins ($C_2^=$-$C_4^=$) increased. At a low GHSV of 1000 Nml*g^{-1}*h^{-1}, over the PM-Na-FeC_x catalyst with a steady-state phase composition, CO_2 conversion increased to 30%, both the selectivity for methane and the selectivity for CO can be controlled below 20%, and the selectivity for light olefins can be boosted to more than 40%. However, low GHSV also led to more significant oxidation of the catalyst. When the operation returned to a GHSV of 6000 Nml*g^{-1}*h^{-1}, the CO_2 conversion decreased, and the CO selectivity increased, as shown in Table S5. The deactivation caused by deep oxidation here may result from increased water vapor generation at low GHSV, which disrupted the dynamic balance of iron oxide and iron carbide inside the iron catalyst.

Considering the different product selectivity and CO_2 conversion on the iron carbide catalyst with and without sodium modification, along with the relationship between product formation discussed above, a simple schematic diagram of product formation during CO_2 hydrogenation over iron carbide catalysts was proposed, as shown in Figure 10C. Over the Fe_5C_2 catalyst, both CH_4 and CO were primary products, produced from initial reaction paths (a) and (b). CO could be further converted into C_{2+} hydrocarbons (c) and CH_4 (d) through Fischer-Tropsch synthesis (FTS) reaction over the active FeC_x component. A higher Fe_5C_2 composition results in a higher CO_2 conversion and higher selectivity for CH_4 and C_{2+} hydrocarbons. Once the iron carbide (Fe_5C_2) was oxidized to iron oxide (Fe_3O_4), both the activities for the FTS (path c) and methanation (path a, d) were weakened, while the reactivity of RWGS became dominant (b). This led to a decrease in the conversion of CO_2 and CO, causing CO to accumulate and resulting in decreased selectivity for both CH_4 and all other hydrocarbons. As a result, the pure Fe_3O_4 catalyst exhibited

very high selectivity for CO. When Na_2CO_3 and iron carbide formed a sufficiently intimate interface, H_2 molecular dissociation was supposed to be suppressed on the surface of the sodium-modified iron carbide catalyst (PM-Na-FeC_x) [12,14], resulting in a decreased CO_2 conversion. At the same time, limited hydrogen dissociation inhibited the rapid formation of CH_4 from direct hydrogenation of CO_2 (path a) and CO (path b), making CO the primary product. The accumulated CO was further converted via the classic CO-FTS reaction, especially under low GHSV, thereby improving the selectivity for C_{2+} hydrocarbons. Moreover, Na_2CO_3 dopants also inhibited the deep hydrogenation of olefins on the surface of the catalysts, resulting in a higher selectivity for light olefins on the sodium-modified iron carbide catalyst.

In summary, two factors can explain the high CO selectivity over the sodium-modified iron carbide catalyst at high GHSV. Firstly, the dopant Na_2CO_3 accelerated the oxidation of iron carbide into iron oxide during CO_2 hydrogenation, which resulted in a decrease in the effective catalyst component responsible for olefin production. Secondly, Na^+ was supposed to alter the dissociation of H_2 on the surface of iron carbide [12,14], slowing down the reaction rate of the CO-based FTS reaction, which led to the accumulation of intermediate CO in CO_2 hydrogenation and an increased selectivity for CO in the final product. Decreasing the space velocity (GHSV) of the reactants can increase the conversion of CO_2 and CO, thereby reducing the selectivity for CO and maintaining a high olefin yield. However, the increased CO_2 conversion resulting from the lower GHSV also produced more water, disrupting the dynamic phase balance between iron carbide and iron oxide. This further led to oxidative deactivation of the iron carbide catalyst, especially the Na-modified iron carbide catalyst under a low GHSV condition.

In the future development of efficient iron-based catalysts for the hydrogenation of CO_2 to light olefins, studying the phase stability of the catalyst will be crucial. Avoiding oxidation and maintaining its carbonized state will undoubtedly be a key focus of further research. Our work revealed that the active center for olefin production originates from the interface between the iron carbide and the alkali metal additive. Therefore, it may be simpler to exclude the alkali metal additive and focus on the stability of the iron-based catalyst alone. Additionally, this work also confirmed that low space velocity accelerates the oxidation of the iron catalyst. This condition can be used to design accelerated oxidation experiments to speed up the screening of more suitable iron-based catalysts in future studies.

Conclusions

In this study, two pure-phase nanostructured Fe_5C_2 and Fe_3O_4 catalysts, with and without Na_2CO_3 dopant, were prepared and evaluated for CO_2 hydrogenation to light olefins. The results indicated a dynamic phase transition between the Fe_5C_2 and Fe_3O_4 phases in the iron-based catalysts, with varying activities during CO_2 hydrogenation. The efficiency of this transformation, between Fe_3O_4 and Fe_5C_2, is strongly influenced by particle size and reaction conditions. Nanosized Fe_5C_2 was easily oxidized to Fe_3O_4 by H_2O and CO_2, causing particle sintering, reduced CO_2 conversion, and increased CO selectivity. However, only small Fe_3O_4 particles were re-carburized to iron carbide by CO and H_2, partially restoring catalytic activity. Therefore, during the CO_2 hydrogenation reaction, with both oxidizing and reducing atmospheres, the Fe_5C_2 and Fe_3O_4 components eventually reach a dynamic phase equilibrium. This equilibrium results in catalytic behavior characterized by an initial decline in activity, followed by stabilization towards a pseudo-steady state.

By physically mixing Fe_5C_2 and Na_2CO_3 and controlling their contact distance, the results showed that closer proximity of Na_2CO_3 and Fe_5C_2 contributed to a higher yield of light olefins during CO_2 hydrogenation. However, Na_2CO_3 also promoted oxidation of the Fe_5C_2 and influenced the phase equilibrium inside iron-based catalysts. Besides, the Na_2CO_3 dopant was supposed to inhibit the dissociation and adsorption of H_2 on the surface of the iron carbide catalyst. This suppression reduced the rapid methanation of both CO_2 and CO, it also inhibited the further hydrogenation of olefins. Nevertheless, the inhibition of hydrogen dissociation also slowed down the CO-mediated FTS synthesis. Combined with the phase oxidation from Fe_5C_2 to Fe_3O_4, this effect ultimately increased CO selectivity over the Na_2CO_3-modified Fe_5C_2 catalyst. Operating at low gas space velocity (GHSV) can be used to reduce CO selectivity while maintaining high selectivity for light olefins by enhancing the extent of the CO-FTS reaction. However, the low GHSV also accelerated the oxidation of Fe_5C_2 to Fe_3O_4, resulting in oxidative deactivation of the iron carbide catalyst.

Conflicts of interest

There are no conflicts to declare.

Data availability

The data supporting this article have been included in the text and as part of the Supplementary information. Should any data files be needed in another format, they are available from the corresponding author upon reasonable request. See DOI:…….

Acknowledgements

This project was conducted at the Chemical Engineering division, the Competence Centre for Catalysis (KCK), and the Centre for Process Chemical Engineering (CPE) at Chalmers University of Technology, and was performed in collaboration with Perstorp AB and Josefsson Sustainable Chemistry AB. We gratefully acknowledge the funding from Swedish Energy Agency (P49617-1) and NextGenerationEU (The Recovery and Resilience Facility, RRF). Special acknowledgments are extended to the Advanced Mössbauer Spectroscopy Center at the Dalian Institute of Chemical Physics (Dalian, China) for providing Mössbauer spectroscopy analyses, and to the China Energy National Institute of Clean and Low-Carbon Energy for conducting the in-situ XRD and STEM experiments

References

1 O. A. Ojelade and S. F. Zaman, A review on CO_2 hydrogenation to lower olefins: Understanding the structure-property relationships in heterogeneous catalytic systems, *J.CO₂ Util.*, 2021, **47**, 101506.

2 D. Goud, R. Gupta, R. Maligal-Ganesh and S. C. Peter, Review of catalyst design and mechanistic studies for the production of olefins from anthropogenic CO_2, *ACS Catal.,* 2020, **10** 14258−14282.

3 G. Centi, G. Laquaniello and S. Perathoner, Can We Afford to Waste Carbon Dioxide? Carbon Dioxide as a Valuable Source of Carbon for the Production of Light Olefins, *ChemSusChem.,* 2011, **4**, 1265 – 1273.

4 W. Liu, S. Cheng, H. S. Malhi, X. Gao, Z. Zhang and W. Tu, Hydrogenation of CO_2 to Olefins over Iron-Based Catalysts: A Review, *Catalysts.,* 2022, **12**, 1432.

5 B. Pawelec, N. Mota, R. Guil-López, J. L. G. Fierro and R. M.N. Yerga, Catalysts for the Conversion of CO_2 to Low Molecular Weight Olefins—A Review, *Materials.,* 2021, **14**, 6952.

6 R. Ye, J. Ding, W. Gong, M. D. Argyle, Q. Zhong, Y. Wang, C. K. Russell, Z. Xu, A. G. Russell, Q. Li, M. Fan and Y. G. Yao, CO_2 Hydrogenation to High-Value Products via Heterogeneous Catalysis, *Nat. Commun.*, 2019, **10**, 5698.

7 T. Numpilai, C. K. Cheng, J. Limtrakul and T. Witoon, Recent advances in light olefins production from catalytic hydrogenation of carbon dioxide, *Process Saf. Environ. Prot.*, 2021, **151** 401-427.

8 W. Di, A. Achour, P. H. Ho, S. Ghosh, O. Pajalic, L. Josefsson, L. Olsson and D. Creaser, Modulating the Formation of Coke to Improve the Production of Light Olefins from CO_2 Hydrogenation over In_2O_3 and SSZ-13 Catalysts, *Energy & fuels,* 2023, **37**, 17382–17398.

9 Y. Han, C.Y. Fang, X. W. Ji, J. Wei, Q. J. Ge and J. Sun, Interfacing with carbonaceous potassium promoters boosts catalytic CO_2 hydrogenation of iron, *ACS Catal.*, 2020, **10**, 12098-12108.

10 J. Zhu, P. Wang, X. Zhang, G. Zhang, R. Li, W. Li, T. P. Senftle, W. Liu, J. Wang, Y. Wang and A. Zhang, Dynamic structural evolution of iron catalysts involving competitive oxidation and carburization during CO_2 hydrogenation, *Sci. Adv.,* 2022, **8**, 3629.

11 L. Tang, L. He, Y. Wang, B. Chen, W. Xu, X. Duan and A. H. Lu, Selective fabrication of χ-Fe_5C_2 by interfering surface reactions as a highly efficient and stable Fischer-Tropsch synthesis catalyst, *Appl. Catal. B.,* 2021, **284**, 119753.

12 Q. Yang, V. A. Kondratenko, S. A. Petrov, D. E. Doronkin, E. Saraçi, H. Lund, A. Arinchtein, R. Kraehnert, A. S. Skrypnik, A. A. Matvienko and E. V. Kondratenko, Identifying Performance Descriptors in CO_2 Hydrogenation over Iron-Based Catalysts Promoted with Alkali Metals, *Angew Chem, Int Ed.,* 2022, **61**, 202116517.

13 B. Liang, H. Duan, T. Sun, J. Ma, X. Liu, J. Xu, X. Su, Y. Huang and T. Zhang, Effect of Na promoter on Fe-based catalyst for CO_2 hydrogenation to alkenes, *ACS Sustain. Chem. Eng.,* 2018, **7**, 925-932.

14 P. P. Paalanen and B. M. Weckhuysen, Carbon pathways, sodium-sulfur promotion and identification of iron carbides in iron-based Fischer-Tropsch synthesis, *ChemCatChem.,* 2020, **12**, 4202-4223.

15 C. G. Visconti, M. Martinelli, L. Falbo, A. Infantes-Molina, L. Lietti, P. Forzatti, G. Palo, E. Iaquaniello, B. Picutti and F. Brignoli, CO_2 hydrogenation to lower olefins on a high surface area K-promoted bulk Fe-catalyst, *Appl. Catal. B.,* 2017, **200**, 530-542.

16 M. Albrecht, U. Rodemerck, M. Schneider, M. Bröring, D. Baabe and E. V. Kondratenko, Unexpectedly efficient CO_2 hydrogenation to higher hydrocarbons over non-doped Fe_2O_3, *Appl. Catal. B.,* 2017, **204**, 119-126.

17 Y. Zhang, C. Cao, C. Zhang, Z. Zhang, X. Liu, Z. Yang, M. Zhu, B. Meng, J. Xu and Y. F. Han, The study of structure-performance relationship of iron catalyst during a full life cycle for CO_2 hydrogenation, *J. Catal.,* 2019, **378**, 51-62.

18 B. Y. Chen, G. Dobele, A. Plavniece, A. Volperts, L. Tamasauskaite-Tamasiunaite, E. Norkus, C. L. Chen and Y. C. Lin, Catalytic hydrogenation of CO_2 to light olefins by using K-doped FeC_x catalysts derived from the Fe-chitosan complex, *Int. J. Hydrog. Energy.,* 2023, **48**, 4276-4286.

19 J. I. Orege, N. Liu, C. C. Amoo, J. Wei, Q. Ge and J. Sun, Boosting CO_2 hydrogenation to high-value olefins with highly stable performance over Ba and Na co-modified Fe catalyst, *J. Energy Chem.*, 2023, **80**, 614-624.

20 Z. Feng, J. Zhao, F. E. Huggins and G. P. Huffman, Agglomeration and phase transition of a nanophase iron oxide catalyst, *J. Catal.,* 1993, **143**, 510-519.

21 D. E. Miser, E. J. Shin, M.R. Hajaligol and F. Rasouli, STEM characterization of phase changes and the occurrence of maghemite during catalysis by an iron oxide, *Appl. Catal. A.,* 2004, **258**, 7-16.

22 E. J. Shin, D. E. Miser, W. G. Chan and M. R. Hajaligol, Catalytic cracking of catechols and hydroquinones in the presence of nano-particle iron oxide, *Appl. Catal. B.,* 2005, **61**, 79-89.

23 D. Mahajan, P. Gütlich, J. Ensling, K. Pandya, U. Stumm and P. Vijayaraghavan, Evaluation of nanosized iron in slurry-phase Fischer − Tropsch synthesis, *Energy & fuels,* 2003, **17**, 1210-1221.

24 C. Yang, H. Zhao, Y. Hou and D. Ma, Fe_5C_2 nanoparticles: A facile bromide-induced synthesis and as an active phase for Fischer–Tropsch synthesis*, J. Am. Chem. Soc.,* 2012, **134**, 15814-15821.

25 F. J. Berry, S. Skinner and M.F. Thomas, Mössbauer spectroscopic examination of a single crystal of Fe_3O_4, *J. Phys.: Condens. Matter.,* 1998, **10**, 215-220.

26 H. Yang, Y. Dang, X. Cui, X. Bu, J. Li, S. Li, Y. Sun and P. Gao, Selective synthesis of olefins via CO_2 hydrogenation over transition-metal-doped iron-based catalysts, *Appl. Catal. B.,* 2023, **321**, 122050.

27 M. K. Khan, P. Butolia, H. Jo, M. Irshad, D. Han, K. W. Nam and J. Kim, Selective conversion of carbon dioxide into liquid hydrocarbons and long-chain α-olefins over Fe-Amorphous AlO_x bifunctional catalysts, *ACS Catal.,* 2020, **10**, 10325-10338.

28 T. Riedel, H. Schulz, G. Schaub, K. W. Jun, J. S. Hwang and K.W. Lee, Fischer–Tropsch on iron with H_2/CO and H_2/CO_2 as synthesis gases: the episodes of formation of the Fischer–Tropsch regime and construction of the catalyst, *Top. Catal.,* 2003, **26**, 41-54.

29 M. Hermanek, R. Zboril, M. Mashlan, L. Machala and O. Schneeweiss, Thermal behavior of iron (II) oxalate dihydrate in the atmosphere of its conversion gases, *J. Mater. Chem.,* 2006,**16**, 1273-1280.

30 J. Zhu, M. Mu, Y. Liu, M. Zhang, G. Zhang, Z. Cheng, B. H. Yin, A. C. Yip, C. Song and X. Guo, Unveiling the promoting effect of potassium on the structural evolution of iron catalysts during CO_2 hydrogenation, *Chem. Eng. Sci.,* 2023, **282**, 119228.

31 J. B. Li, H. F. Ma, H. T. Zhang, Q. W. Sun, W. Y. Ying, & D. Y Fang, Direct production of light olefins from syngas over potassium modified Fe–Mn catalyst. *React. Kinet. Mech. Catal.,* 2014,**112,** 409-423.

32 H. Wan, B. Wu, C. Zhang, H. Xiang, & Y. Li, Promotional effects of Cu and K on precipitated iron-based catalysts for Fischer–Tropsch synthesis. *J. Mol. Catal. A:Chem.,* 2008, **283,** 33-42.

View Article Online
DOI: 10.1039/D6TA00959J

Dear Editors for *Journal of Materials Chemistry A*,

I confirm that the data supporting this study are available as described below.

The data herein includes the data collected and analyzed to support this study, including the data underlying the main text and the supplementary materials. All data have been packaged as a single dataset and deposited in the Zenodo repository. The dataset is publicly available at the following DOI: https://doi.org/10.5281/zenodo.18310645

Best regards

Sincerely,

Louise Olsson (Corresponding author)

Chemical Engineering division,

Chalmers University of Technology

louise.olsson@chalmers.se